[28] Buyens K, Meyer M, Wagner E, Demeester J, De Smedt SC, Sanders NN. Monitoring the disassembly of siRNA polyplexes in serum is crucial for predicting their biological efficacy. J Control Release 2010;141:38–41.
[29] Nakanishi M, Park JS, Jang WD, Oba M, Kataoka K. Study of the quantitative aminolysis reaction of poly(β-benzyl L-aspartate) (PBLA) as a platform polymer for functionality materials. React Funct Polym 2007;67:1361–72.
[30] Oba M, Fukushima S, Kanayama N, Aoyagi K, Nishiyama N, Koyama H, et al. Cyclic RGD peptide-conjugated polyplex micelles as a targetable gene delivery system directed to cells possessing $\alpha_v\beta_3$ and $\alpha_v\beta_5$ integrins. Bioconjug Chem 2007;18:1415–23.
[31] Zhao H, Sterner ES, Coughlin EB, Theato P. o-Nitrobenzyl alcohol derivatives: opportunities in polymer and materials science. Macromolecules 2012;45:1723–36.
[32] Miguel VS, Bochet CG, Compo A. Wavelength-selective caged surfaces: how many functional levels are possible? J Am Chem Soc 2011;133:5380–8.
[33] Harris JR, Roos C, Djalali R, Rheingans O, Maskos M, Schmidt M. Application of the negative staining technique to both aqueous and organic solvent solutions of polymer particles. Micron 1999;30:289–98.
[34] Zhulina EB, Borisov OV. Theory of block polymer micelles: recent advances and current challenges. Macromolecules 2012;45:4429–40.
[35] Fukushima S, Miyata K, Nishiyama N, Kanayama N, Yamasaki Y, Kataoka K. PEGylated polyplex micelles from triblock cationers with spatially ordered layering of condensed pDNA and buffering units for enhanced intracellular gene delivery. J Am Chem Soc 2005;127:2810–1.
[36] Miyata K, Oba M, Kano MR, Fukushima S, Vachutinsky Y, Han M, et al. Polyplex micelles from triblock copolymers composed of tandemly aligned segments with biocompatible, endosomal escaping, and DNA-condensing functions for systemic gene delivery to pancreatic tumor. Pharm Res 2008;25:2924–36.
[37] Xu X, Smith AE, Kirkland SE, McCormick CL. Aqueous RAFT synthesis of pH-responsive triblock copolymer mPEO-PAPMA-PDPAEMA and formation of shell cross-linked micelles. Macromolecules 2008;41:8429–35.
[38] Jiang X, Zhang G, Narain R, Liu S. Fabrication of two types of shell-cross-linked micelles with "inverted" structures in aqueous solution from schizophrenic water-soluble ABC triblock copolymer via click chemistry. Langmuir 2009;25:2046–54.
[39] Itaka K, Kataoka K. Recent development of nonviral gene delivery systems with virus-like structures and mechanisms. Eur J Pharm Biopharm 2009;71:475–83.
[40] Chen H, Kim S, Li L, Wang S, Park K, Cheng JX. Release of hydrophobic molecules from polymer micelles into cell membranes revealed by Forster resonance energy transfer imaging. Proc Natl Acad Sci U S A 2008;105:6596–601.

Journal of Controlled Release 178 (2014) 18–24

Contents lists available at ScienceDirect

Journal of Controlled Release

journal homepage: www.elsevier.com/locate/jconrel

Systemic siRNA delivery to a spontaneous pancreatic tumor model in transgenic mice by PEGylated calcium phosphate hybrid micelles

Frederico Pittella [a,b], Horacio Cabral [b], Yoshinori Maeda [b], Peng Mi [c], Sumiyo Watanabe [a], Hiroyasu Takemoto [c], Hyun Jin Kim [d], Nobuhiro Nishiyama [c], Kanjiro Miyata [a,*], Kazunori Kataoka [a,b,d,e,**]

[a] Center for Disease Biology and Integrative Medicine, Graduate School of Medicine, The University of Tokyo, 7-3-1 Hongo, Bunkyo-ku, Tokyo 113-0033, Japan
[b] Department of Bioengineering, Graduate School of Engineering, The University of Tokyo, 7-3-1 Hongo, Bunkyo-ku, Tokyo 113-8656, Japan
[c] Polymer Chemistry Division, Chemical Resources Laboratory, Tokyo Institute of Technology, R1-11, 4259 Nagatsuta, Midori-ku, Yokohama 226-8503, Japan
[d] Department of Materials Engineering, Graduate School of Engineering, The University of Tokyo, 7-3-1 Hongo, Bunkyo-ku, Tokyo 113-8656, Japan
[e] Center for NanoBio Integration, The University of Tokyo, 7-3-1 Hongo, Bunkyo-ku, Tokyo 113-8656, Japan

ARTICLE INFO

Article history:
Received 3 August 2013
Accepted 7 January 2014
Available online 15 January 2014

Keywords:
siRNA delivery
Calcium phosphate
PEG
Charge-conversional polymer
Transgenic mice
Spontaneous pancreatic carcinoma

ABSTRACT

Efficient systems for delivery of small interfering RNA (siRNA) are required for clinical application of RNA interference (RNAi) in cancer therapy. Herein, we developed a safe and efficient nanocarrier comprising poly(ethylene glycol)-*block*-charge-conversional polymer (PEG-CCP)/calcium phosphate (CaP) hybrid micelles for systemic delivery of siRNA and studied their efficacy in spontaneous bioluminescent pancreatic tumors from transgenic mice. PEG-CCP was engineered to provide the siRNA-loaded hybrid micelles with enhanced colloidal stability and biocompatibility due to the PEG capsule and with endosome-disrupting functionality due to the acidic pH-responsive CCP segment where the polyanionic structure could be converted to polycationic structure at acidic pH through *cis*-aconitic amide cleavage. The resulting hybrid micelles were confirmed to have a diameter of <50 nm, with a narrow size distribution. Intravenously injected hybrid micelles significantly reduced the luciferase-based luminescent signal from the spontaneous pancreatic tumors in an siRNA sequence-specific manner. The gene silencing activity of the hybrid micelles correlated with their preferential tumor accumulation, as indicated by fluorescence imaging and histological analysis. Moreover, there were no significant changes in hematological parameters in mice treated with the hybrid micelles. These results demonstrate the great potential of the hybrid micelles as siRNA carriers for RNAi-based cancer therapy.

1. Introduction

Small interfering ribonucleic acid (siRNA) provides new perspectives for the treatment of various diseases. It functions by obstructing a specific cellular process by reducing protein production in a sequence-specific manner, a phenomenon termed RNA interference (RNAi) [1–4]. In particular, the use of RNAi-based therapy is expected to have potential for treatment of cancer because cancerous cells overexpress several specific genes, including oncogenes [5,6]. In the development of an RNAi-based cancer therapy, systemic administration of siRNA is essential for its effective accumulation in the wide range of internal tumor tissues. However, intravenous injection of naked siRNA molecules results in their rapid enzymatic degradation and subsequent clearance through the kidneys [7,8]. Therefore, efficient carriers are required to ensure successful delivery of siRNA to the therapeutic site of action [3,6,9].

Calcium phosphate (CaP)-based nanocarriers, a promising delivery system, has been widely developed for delivering nucleic acids to mammalian cells [10–14]. These are readily prepared by mixing aqueous ionic solutions for efficient encapsulation of nucleic acids. In this regard, we have previously prepared poly(ethylene glycol) (PEG)-coated CaP hybrid micelles by utilizing PEG-polyanion block copolymers [12,15–20]. In these block copolymers, the polyanion segment acts as a binding moiety with CaP nanoparticles, whereas the PEG segment forms a nonionic and hydrophilic outer layer for enhanced colloidal stability and biocompatibility (Fig. 1A). Furthermore, our recent studies successfully demonstrated functionalization of the polyanion segment for efficient endosomal escape of the siRNA payload [19–21]. An acidic pH-responsive anionic moiety, *cis*-aconitic amide (Aco), was introduced into the cationic side chain of the endosome-disrupting polyaspartamide derivative, poly{*N*′-[*N*-(2-aminoethyl)-2-aminoethyl] aspartamide} (PAsp(DET)) (Fig. 1B). The obtained PAsp(DET-Aco) bearing a net negative charge was found to be inactive for membrane disruption at extracellular neutral pH. However, on reversion to the parent polycation PAsp(DET) by cleavage of the Aco moiety at endosomal acidic pH, membrane disruptivity was activated [thus, termed charge-conversional polymer (CCP)] (Fig. 1C) [22]. Ultimately, the systemic administration of PEG-CCP/CaP hybrid micelles carrying

* Corresponding author. Tel.: +81 3 5841 1701; fax: +81 3 5841 7139.
** Correspondence to: K. Kataoka, Center for Disease Biology and Integrative Medicine, Graduate School of Medicine, The University of Tokyo, 7-3-1 Hongo, Bunkyo-ku, Tokyo 113-0033, Japan. Tel.: +81 3 5841 7138; fax: +81 3 5841 7139.
E-mail addresses: miyata@bmw.t.u-tokyo.ac.jp (K. Miyata), kataoka@bmw.t.u-tokyo.ac.jp (K. Kataoka).

0168-3659/$ – see front matter © 2014 Elsevier B.V. All rights reserved.
http://dx.doi.org/10.1016/j.jconrel.2014.01.008

vascular endothelial growth factor (VEGF) siRNA achieved significant antitumor activity in a murine xenograft model of subcutaneous pancreatic tumors [20]. These results demonstrated the great potential of this system for use as a cancer therapy and motivated us to investigate this system further.

To confirm the translational capability of promising nanocarriers, relevant preclinical tumor models, which parallel the microenvironment characteristics of tumors in the clinic, should be considered. In animal tumor models prepared by implantation of exogenous cancer cells or tissues, the tumoral microenvironment presents substantial differences with that of tumors in patients, including stroma, vasculature, lymphatics, immune cells, and increased population of certain clonal fractions due to selective stresses during cell culture or tissue transplantation [23,24]. These features in transplanted models are expected to affect the nanocarrier-mediated delivery of siRNA as well as drugs, *e.g.*, efficiencies of penetration, accumulation, and gene silencing in tumor tissues. In this regard, in genetically engineered tumor models, the tumor development closely relates to the clinical setting of the disease, with immune responses, angiogenesis, and inflammation naturally interrelating with the tumor [23]. Therefore, by using such spontaneous tumor models, siRNA-loaded nanocarriers could be evaluated in tumors with more relevant microenvironment and cell populations.

In the present study, we applied siRNA-loaded hybrid micelles in a genetically engineered pancreatic tumor model, in which the tumor gradually arises *in situ* and is associated with normal immune, angiogenesis, and inflammatory processes. The EL1-Luc/TAg transgenic mice used in this study spontaneously develop bioluminescent pancreatic adenocarcinoma owing to the SV40 T and firefly luciferase transgene constructs, which are regulated by the rat EL1 promoter [25]. SV40 T alters molecular, physiological, and histological aspects comparable to the tumorigenesis of acinar cell carcinoma in humans. Moreover, EL1-Luc/TAg transgenic mice permit non-invasive tracing of tumors through bioluminescence imaging because the cancer cells exclusively express luciferase. Accordingly, *in vivo* RNAi activity of the hybrid micelles carrying luciferase siRNA (siLuc) was determined by quantifying the luminescent signal from the pancreatic tumors after intravenous injection. To verify the validity of the measured RNAi activity, the tumor accumulation profile of the hybrid micelles was further assessed. To the best of our knowledge, this is the first study to demonstrate the effective delivery of siRNA to a spontaneous tumor model in transgenic mice by systemic administration.

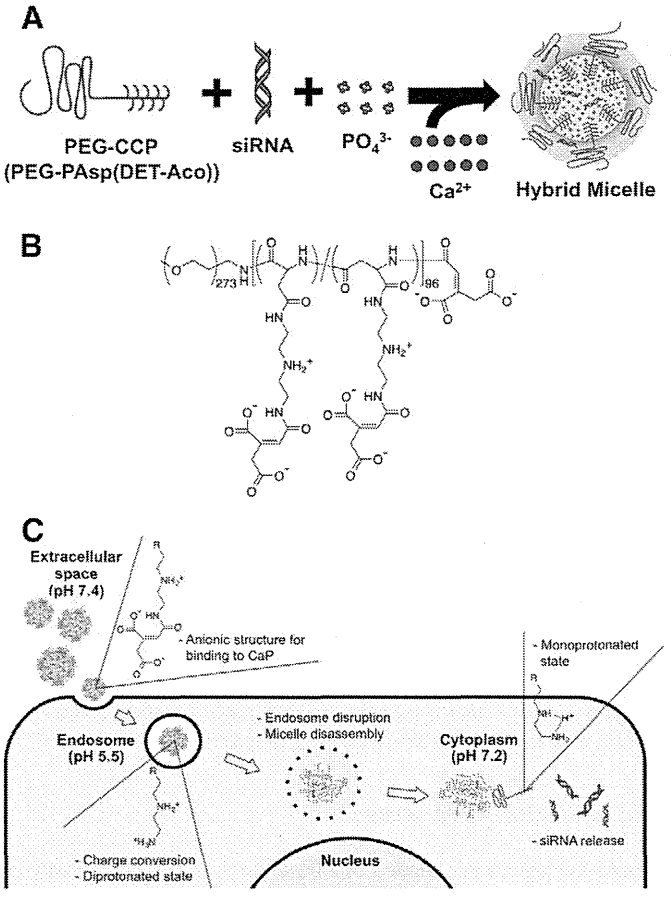

Fig. 1. (A) Schematic illustration of the preparation of hybrid micelles with PEG-CCP, siRNA, and CaP. (B) Chemical structure of PEG-PAsp(DET-Aco), termed PEG-CCP. (C) Schematic illustration of the cellular delivery of siRNA by PEG-CCP/CaP hybrid micelles. At extracellular neutral pH, PEG-CCP binds to the CaP nanoparticle, generating a PEG outer layer. Once endocytosed by the cell, the hybrid micelles undergo endosomal acidification. During acidification, PEG-CCP is converted to the parent PEG-PAsp(DET) through cleavage of the *cis*-aconitic amide bond, exposing the diprotonated side chain structure for endosomal membrane disruption. Finally, the siRNA payload is released into the cytoplasm, while the PAsp(DET) segment adopts the membrane-inactive monoprotonated side chain at cytoplasmic neutral pH.

2. Materials and methods

2.1. Materials, cell lines, and animals

$CaCl_2$ (anhydrous), Na_3PO_4, NaCl, HCl, ethanol, and phosphate buffered saline (PBS) were purchased from Wako Pure Chemical Industries Ltd. (Osaka, Japan). Dulbecco's modified Eagle's medium (DMEM) and penicillin/streptomycin stabilized solution were purchased from Sigma-Aldrich (St. Louis, MO). *In vivo* grade luciferin VivoGlo, cell culture lysis buffer, and the Luciferase Assay System were purchased from Promega Corporation (Madison, WI). Tissue-Tek OCT compound and fetal bovine serum (FBS) were acquired from Sakura Finetek USA, Inc. (Torrance, CA) and Dainippon Sumitomo Pharma Co., Ltd. (Osaka, Japan), respectively. Methoxy-poly(ethylene glycol)-*block*-poly(*N*″-{*N*′-[(*N*-*cis*-aconityl)-2-aminoethyl]-2-aminoethyl}aspartamide) (PEG-PAsp(DET-Aco) or PEG-CCP) was synthesized as previously described, and then characterized by ^{1}H NMR (PEG: 12 kDa; PAsp(DET-Aco): 34 kDa) [19,20]. Firefly luciferase siRNA (siLuc) and its control siRNA (siScr) were synthesized by Hokkaido System Science (Hokkaido, Japan). The sequences of the siLuc were: 5′-CUU ACG CUG AGU ACU UCG AdTdT-3′ (sense) and 5′-UCG AAG UAC UCA GCG UAA GdTdT-3′ (antisense); the sequences of the siScr were: 5′-UUC UCC GAA CGU GUC ACG UdTdT-3′ (sense) and 5′-ACG UGA CAC GUU CGG AGA AdTdT-3′ (antisense). Fluorescently labeled siLuc was obtained by introducing Alexa Fluor 647 to the 5′ end of sense strand from GeneDesign, Inc. (Osaka, Japan).

HeLa-Luc, a firefly luciferase-expressing human cervical cancer cell line, was purchased from Caliper Life Science (Hopkinton, MA). The cells were maintained in DMEM containing 10% FBS and 1% streptomycin/penicillin in a humidified atmosphere containing 5% CO_2 at 37 °C. FVB/NJc1 female mice (18–20 g, 6 weeks) were purchased from Clea Japan, Inc. (Tokyo, Japan). EL1-Luc/EL1-SV40 T-antigen transgenic mice (OncoMouse; male, 18–20 g, 6 weeks) were purchased from Caliper Life Sciences (Hopkinton, MA). Female FVB mice and male transgenic mice were allowed to breed, and the newborn mice were genotyped primarily by basal bioluminescence imaging at the age of 5 weeks. Male mice presenting basal luminescence in the pancreas were separated for use in the experiments. All animal experiments were performed in accordance with the Guidelines for the Care and Use of Laboratory Animals as stated by The University of Tokyo.

2.2. Preparation of hybrid micelles

Hybrid micelles were prepared as previously described [20]. In brief, a solution of 2.5 M $CaCl_2$ (1 μL) was diluted in 10 mM Tris buffer (pH 10) (11.5 μL). Another solution containing PEG-CCP (1.0 mg/mL) in 10 mM Tris/HCl buffer (pH 7.5) was mixed with a solution of 15 μM siRNA in 10 mM HEPES buffer (pH 7.2) and with 50 mM HEPES buffer containing 1.5

mM Na_3PO_4 and 140 mM NaCl (pH 7.5) (2.5 μL:5 μL:5 μL). The former solution was mixed with the latter solution by pipetting up and down for approximately 20 s (final siRNA concentration: 3 μM). The freshly prepared micelle solution containing 40 μg siRNA and 100 μg PEG-CCP (1 mL) was then purified and concentrated using a VivaSpin-06 device (molecular weight cut-off (MWCO): 10 kDa). The ultrafiltration was performed in a swing bucket rotor at 900 *g* and 4 °C for 20 min. To minimize non-specific binding of micelles to the membrane, the centrifuge filter devices were washed with de-ionized water before use. After centrifugation, the retained solution (100 μL) was added to 300 mM NaCl solution (100 μL) to adjust the final concentration to 150 mM NaCl. Through this procedure, the excess free calcium ions were removed from the micelle solution to the flow-through. The quantity of calcium removed was determined using a calcium sensitive dye, arsenazo III, by the SRL Laboratories (SRL Inc., Tokyo, Japan).

2.3. Transmission electron microscopic (TEM) imaging

Hybrid micelle solution (20 μL) was loaded on a 400-mesh copper grid and stained with 20 μL of uranyl acetate solution (2%, w/v) for 5 s. The copper grids with carbon-coated collodion film were glow-discharged for 10 s with an Eiko IB-3 ion coater (Eiko Engineering Co. Ltd., Japan) prior to use. The morphology of hybrid micelles was observed on a JEM-1400 (JEOL Ltd., Tokyo, Japan) with 100 kV acceleration voltage and 40 μA beam current, toward high resolution and high contrast with high performance imaging of specimens.

2.4. In vitro luciferase gene silencing

HeLa-Luc cells were seeded in a 96-well plate at a cell density of 2500 cells/well in 0.1 mL of DMEM containing 10% FBS and then pre-cultured for 24 h. Before transfection, the medium was refreshed. Hybrid micelles containing siRNA (siLuc or siScr), hybrid micelles without siRNA (mock), or naked siRNA (siLuc or siScr) were applied to each well to final siRNA concentrations of 100 and 200 nM (n = 6). After 48 h of incubation, the medium was removed and the cells were washed twice with 100 μL of PBS. The cells were then lysed with 50 μL of cell culture lysis buffer. The luciferase expression in the lysate was determined from photoluminescence intensity using the Luciferase Assay System and Mithras LB 940 (Berthold Technologies). The relative luciferase activity was calculated as a ratio to that in non-treated cells.

2.5. Biodistribution and tumor accumulation of hybrid micelles in transgenic mice

Mice were fed with alfalfa-free food *ad libitum*. A group of three male transgenic mice (15 weeks) were intravenously injected with Alexa Fluor 647-labeled siLuc (Alexa647-siLuc) contained in hybrid micelles (200 μL, 20 μg siRNA). As a control, the same amount of naked Alexa647-siLuc was also injected to another group of male transgenic mice. Intravenous injection was performed slowly (10 s per injection) to avoid adverse side effects. Mice were sacrificed 6 h after the injection, and then the main organs (heart, lungs, liver, spleen, kidneys, and pancreas, including tumors) were excised for fluorescent imaging using IVIS (Caliper Life Sciences, Hopkinton, MA). Organs were washed in PBS and kept on ice prior to analysis. Similarly, blood was collected from mice at 6 h after the injection, and then it was centrifuged at 2000 *g* for 10 min to obtain the plasma. The fluorescence intensity was determined using the Living Image software through the selection of an ROI around the whole organ/tumor and the plasma, and then it was converted to the % of dose/g of tissue (or plasma) based on a standard curve. To avoid incomplete separation of tumors from the pancreas, the combined weight of the organ and tumors was used for the subsequent statistical data analysis.

2.6. Tumor histology

After the biodistribution studies described in the preceding section were complete, a portion of the pancreas/tumor tissue from each mouse was rapidly frozen in Tissue-Tek OCT compound with liquid nitrogen in ethanol. The frozen pancreas/tumor tissues embedded in the block were then cut into 6-μm thick slices at −20 °C with a Tissue-Tek Cryo3 microtome/cryostat (Sakura Finetek USA, Inc., Torrance, CA). Each section of the pancreas/tumor tissue was fixed with formalin and stained with hematoxylin and eosin (HE) for histological identification of tumor cells and healthy pancreatic cells. In addition to HE staining, adjacent cryosections of the pancreas/tumor tissue were stained with Hoechst 33342 (Dojindo Lab., Kumamoto, Japan) for observation of cellular nuclei using a confocal laser scanning microscope (CLSM) (LSM 510, Carl Zeiss, Germany). The CLSM observation was performed at the excitation wavelengths of 633 nm (He–Ne laser) and 710 nm (MaiTai laser, two photon excitation) for Alexa647-siRNA and Hoechst 33342, respectively. The fluorescence intensities of the Alexa647-siRNA from the tumor region or the healthy pancreatic region in the obtained CLSM image were determined using the ImageJ software.

2.7. In vivo luminescence reduction in transgenic mice

Hybrid micelle solutions containing 20 μg of siLuc or siScr (200 μL) were slowly injected into the caudal vein of transgenic mice (13 weeks; n = 16). Bioluminescence intensity in the pancreatic tumors was determined before injection and 24 h after injection of the hybrid micelles using an IVIS instrument. Mice were anesthetized with isoflurane and luciferin was injected intraperitoneally at a dosage of 150 mg/kg (200 μL). Measurements were performed 10 min after luciferin injection for three different positions in each mouse (right flank, left flank, and ventral positions) to reduce variability in bioluminescence due to the tumor positions. Photons emitted from the pancreas region were quantified using the Living Image software and summed from the 3 positions. All images were set to the same conditions and color scale.

2.8. Hematological parameters and cytokine levels

Hybrid micelle solutions containing 20 μg of siScr (200 μL) were slowly injected in the caudal vein of female Balb/c mice (6 weeks). Blood was collected at several time points after the injection and centrifuged at 2000 *g* for 10 min to obtain the plasma. The levels of alkaline phosphatase (ALP), aspartate aminotransferase (AST), alanine aminotransferase (ALT), and creatinine (Cr) in the plasma were measured by the SRL Laboratories (SRL Inc., Tokyo, Japan) (n = 5). Also, the levels of tumor necrosis factor-α (TNF-α), interleukin-6 (IL-6), IL-1α, and IL-1β in plasma were determined by Quantikine® ELISA kits, according to the manufacturer's protocol (n = 4).

3. Results and discussion

3.1. Preparation of hybrid micelles

Preparation of CaP nanoparticles in an aqueous solution is known to result in the formation of insoluble large aggregates over time. Thus, PEG-CCP (Fig. 1B) was used to prepare CaP nanoparticles with enhanced colloidal stability through the steric repulsive effect of the PEG capsule. These nanoparticles also had endosome-disrupting functionality derived from the CCP segment. This segment was synthesized through the introduction of an Aco moiety into the side chain of PAsp(DET) through *cis*-aconitic amide bond formation. Successful preparation of PEG-CCP (or quantitative introduction of the Aco moiety) was confirmed using ^{1}H NMR spectroscopy (data not shown), as previously described [19]. The resulting PAsp(DET-Aco) segment was stable at neutral pH, whereas under acidic conditions, it underwent *cis*-aconitic amide cleavage to revert back to the parent PAsp(DET) (Fig. 1C) [22].

The generated PAsp(DET) enabled acidic pH-selective membrane disruption based on the distinctive change in the protonation state of the side chain unit, *i.e.*, the monoprotonated state at neutral pH and the diprotonated state at acidic pH, directed toward endosomal escape of the payload (Fig. 1C) [26,27].

The hybrid micelles were prepared by simple mixing of a solution containing PEG-CCP, siRNA, and phosphate ions, with a solution of calcium ions (Fig. 1A). The prepared micelles were then subjected to ultrafiltration (MWCO: 10 kDa) for the removal of excess free calcium ions as well as for concentration of the sample. The concentrated solution was diluted with the same volume of NaCl solution (300 mM) to generate the hybrid micelle solution at 150 mM NaCl. The obtained hybrid micelles were observed with a high performance TEM. Fig. 2A depicts spherical nanoparticles of approximately 30 nm in diameter with a clearly narrow size distribution, which was confirmed by the size distribution histogram obtained from analyses of the TEM images (mean diameter: 33.2 nm, n = 111) (Fig. 2B). The hybrid micelle solution was further characterized by dynamic light scattering (DLS) and electrophoretic light scattering. The size of hybrid micelles was 38 nm at the peak of the number-weighted histogram in DLS (Supporting Fig. S1), associated with a narrow size distribution (polydispersity index = 0.09). This size is consistent with that estimated from the TEM images. Further, the zeta-potential of hybrid micelles was almost neutral (−2.2 mV), consistent with the presence of nonionic PEG outer layer. In addition, the DLS analysis revealed that the cumulant size of the hybrid micelles was maintained over 7 days of storage at 4 °C (data not shown), demonstrating the potential for long-term storage in a refrigerator.

3.2. In vitro luciferase gene silencing

To confirm *in vitro* siRNA delivery efficacy, the hybrid micelles carrying siLuc were applied to a luciferase assay with cultured HeLa-Luc cells as a luciferase-expressing model cell line. After 48 h of incubation, siLuc delivered by the hybrid micelles significantly decreased the luciferase expression in a dose-dependent manner (Fig. 3); the hybrid micelles inhibited approximately 50% and 90% of luciferase expression at 100 nM and 200 nM siRNA, respectively. In sharp contrast, the hybrid micelles with a control sequence of siRNA (siScr) as well as the mock micelles without siRNA resulted in no reduction in luciferase expression, indicating sequence-specific, potent gene silencing ability of the hybrid micelles. In our previous studies, the hybrid micelles exhibited a significant gene silencing effect on endogenous VEGF in cultured pancreatic cancer cells (PanC-1 and BxPC3) [19,20], suggesting that their gene silencing ability is not limited to a specific target gene and cell line. The efficient gene silencing ability of the hybrid micelles was probably due to the stable encapsulation of siRNA in CaP nanoparticles in cell culture medium [20], followed by efficient cellular internalization and endosomal escape induced by the CCP segment [19]. With regard to the cellular internalization, our previous study revealed that hybrid micelles were efficiently uptaken by HeLa cells within 4 h, probably due to an energy-dependent endocytosis [16]. It should be noted that no significant cytotoxicity was observed for any of the samples at the tested concentrations, as determined in a cell viability assay using a water soluble tetrazolium salt (WST-8) (data not shown).

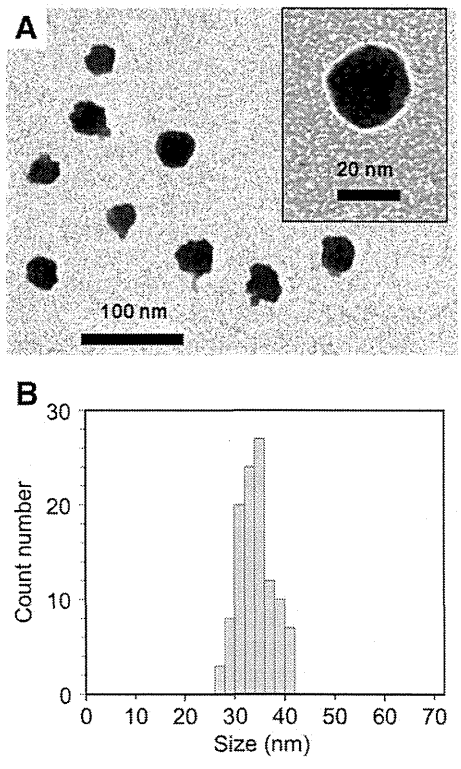

Fig. 2. (A) TEM image of the hybrid micelles. (B) Size distribution histogram of the hybrid micelles based on their TEM images.

3.3. Biodistribution and tumor accumulation of hybrid micelles in transgenic mice

Biodistribution of hybrid micelles after intravenous injection was evaluated in the transgenic mice presenting spontaneous pancreatic tumors using Alexa647-siRNA. At 6 h after injection, the transgenic mice were sacrificed, and the organs were excised for measuring fluorescence intensity, which was then converted to the % of dose/g of tissue based on a standard curve. As the border between a pancreatic tumor and healthy pancreas tissue is unclear, the fluorescence intensity of the whole pancreatic tissue was measured for tumor accumulation of Alexa647-siRNA. Note that the significant fluorescence was not detected from the collected blood samples, indicating that almost all the hybrid micelles (or Alexa647-siRNAs) were eliminated from the bloodstream within 6 h. Thus, the fluorescence intensity measured from each organ would not be affected by blood circulating micelles. As shown in Fig. 4, the amount of hybrid micelles was approximately 0.9% of dose/g of pancreas/tumor, which was 6-fold larger than that in naked siRNA. No significant difference between hybrid micelles and naked siRNA was observed for the accumulation in other organs; however, the kidneys displayed lower accumulation for Alexa647-siRNA delivered by the hybrid micelles compared to naked siRNA. These results suggest that the hybrid micelles could protect Alexa647-siRNA from rapid renal filtration, enabling it to circulate for longer in the blood, and therefore accumulate more in the pancreas/tumor.

The enhanced accumulation of hybrid micelles in the pancreas/tumor was further investigated by histological analysis. First, HE-stained sections were prepared to facilitate distinction of the tumor region (T) from healthy pancreatic tissue (H). As depicted in Fig. 5A, healthy pancreatic cells were organized into lobules toward formation of glandular acini. In contrast, tumor cells show a non-organized solid growth pattern [28,29]. Fig. 5A also shows the presence of connective tissue septa in between the T and H areas. CLSM was then performed to image the corresponding Hoechst 33342-stained sections. It is noteworthy that fluorescence signals from Alexa647-siRNA delivered by hybrid micelles were found mainly in the tumor region (Fig. 5B). Quantitative analysis using the ImageJ software indicated that the fluorescence signal of Alexa647-siRNA in the tumor region was 2.9-fold stronger than that in the healthy pancreas. By considering that the average weight of pancreas/tumor in the transgenic mice was 2.2-fold higher than that of pancreas in wild-type mice, the tumor accumulation of siRNA delivered by hybrid micelles can be roughly estimated to be ~1.3% of dose/g of tumor with the assumption that the tissue weights are similar between tumor and healthy pancreas in the transgenic mice. Thus, the

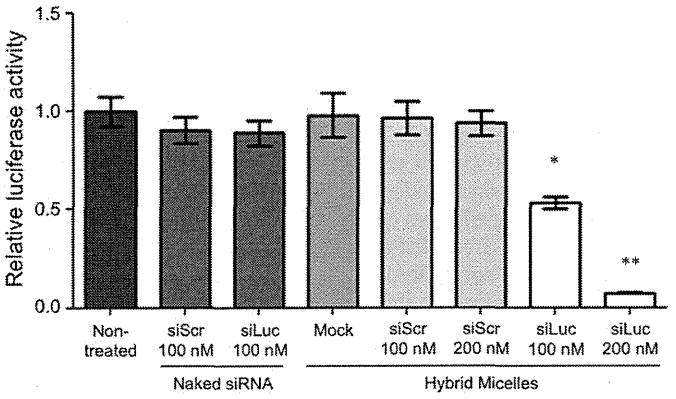

Fig. 3. *In vitro* luciferase gene silencing by hybrid micelles in cultured HeLa-Luc cells. Luciferase luminescence was quantified after 48 h of incubation of cells treated with samples. Results are expressed as mean and standard deviation (n = 6). *$P < 0.05$; **$P < 0.001$ (ANOVA followed by Newman–Keuls).

preferential tumor accumulation of siRNA-loaded hybrid micelles was demonstrated in the spontaneous pancreatic tumor model.

In a previous study, we reported that the tumor vasculature in the EL1-Luc/TAg transgenic mice was covered with pericytes [30], which can considerably limit the penetration of nanocarriers into the spontaneous tumor model in comparison to hypervascular and/or less stromal tumor models [31,32]. Nevertheless, the hybrid micelles apparently penetrated and distributed within the tumors (Fig. 5B). This behavior should be attributed to the relatively small size of the hybrid micelles (approximately 30–40 nm in diameter, Fig. 2 and Supporting Fig. S1), facilitating the passage of the nanocarriers through the tumor vasculature and stromal tissues. This was in agreement with our recent study where <50-nm polymeric micelles efficiently penetrated into the tissue, even in hypopermeable tumor models, which was in contrast to the control micelles that were >50 nm in size [33]. It should be further noted that the enhanced tumor accumulation behavior of hybrid micelles, compared to naked siRNA, in the present spontaneous pancreatic tumors was comparable to our previous observation in a subcutaneous BxPC3 tumor model [20]. This can also be explained by the small size of hybrid micelles, as the small-sized nanocarriers may be less affected by the tumor microenvironments restricting extravasation and penetration of nanocarriers, such as pericyte coverage of the vasculature [33]. Altogether, the hybrid micelles are a promising strategy for the systemic delivery of siRNA to various and whole tumor tissues/cells.

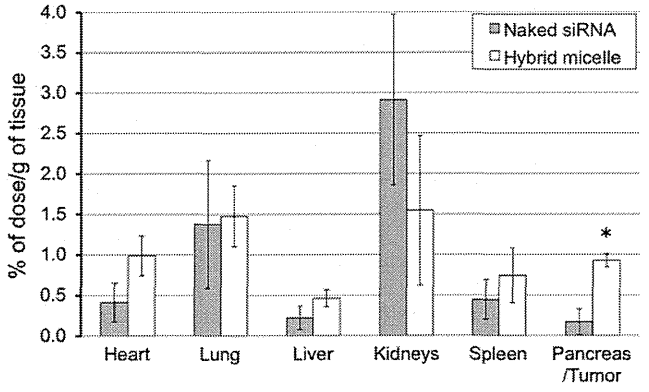

Fig. 4. Biodistribution of Alexa647-siRNA-loaded hybrid micelles and naked Alexa647-siRNA by fluorescence quantification at 6 h after intravenous injection (20 μg siRNA/injection) in 14-week-old transgenic mice. The obtained fluorescence intensities were converted to % of dose/g of tissue based on a standard curve. Results are expressed as mean and standard error of mean (n = 3). ANOVA followed by Newman–Keuls (*$P < 0.01$).

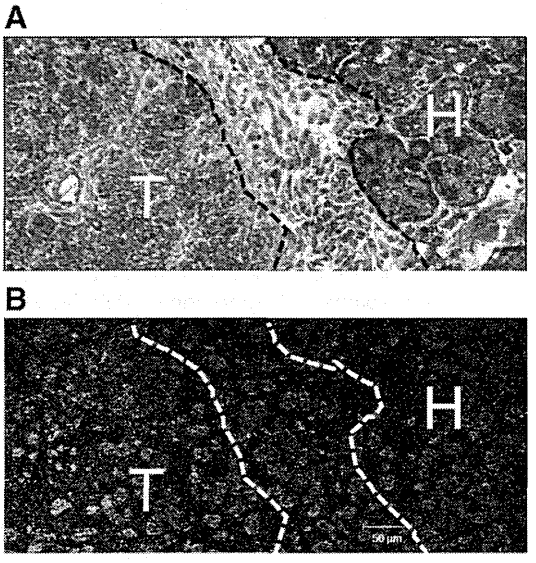

Fig. 5. Histological observation of pancreas/tumor in transgenic mice treated with hybrid micelles. Sections were prepared from the pancreas/tumor tissue excised at 6 h after intravenous injection of hybrid micelles carrying Alexa647-siRNA (20 μg siRNA/injection) to transgenic mice. (A) HE staining: non-organized tumor cells (T) and healthy pancreatic structure in lobes (H) are separated by the dotted line. (B) CLSM image of an adjacent section to that stained with HE. Nuclei (blue) were stained with Hoechst 33342, and Alexa647-siRNA is shown in green.

3.4. In vivo luciferase gene silencing in transgenic mice

Pancreatic cancer is considered to be one of the most fatal cancers [34]. Moreover, the all-stage 5-year survival has not improved greatly during the last 25 years [35]. These facts have motivated us to develop novel therapeutics to improve the prognosis of pancreatic cancer patients. An immunocompetent mouse presenting spontaneous pancreatic tumors is a useful model for establishment of such novel therapeutics, including anticancer drug-loaded micelles [30]. Herein, the *in vivo* gene silencing activity of hybrid micelles was evaluated with the spontaneous pancreatic tumor model developed in EL1-Luc/TAg transgenic mice, in which the expression of firefly luciferase is promoted specifically in the acinar cell carcinoma [25]. Accordingly, this model can be used for a gene silencing assay that employs the bioluminescence of the pancreatic tumors. It is worth noting that the following characteristics were confirmed for the spontaneous pancreatic cancer model in the previous study [30]; i) liver and intestine metastases are likely to occur in this model after the mice becoming 16 weeks old, ii) the pancreas/tumor in this model is enlarged and also the pancreatic cancer may grow over the normal position of pancreas, and iii) the bioluminescent signal from the pancreatic cancer is not always emitted from the same anatomic position. Considering these points, the bioluminescence measurements in this study were performed for 3 different positions, *i.e.*, left flank, frontal, and right flank of the 13-week-old mice without detectable tumor metastases.

Representative bioluminescence images of the left flank position of mice treated with or without siLuc-loaded hybrid micelles are shown in Fig. 6A, where the variable bioluminescence signals from the pancreatic tumor can be identified. At 24 h after systemic injection of the hybrid micelles, the bioluminescence intensity in the pancreatic tumors exhibited a significant reduction of 61% compared with the initial intensity before injection (Fig. 6B; $P < 0.01$), indicating that the hybrid micelles induced efficient luciferase gene silencing in the tumor tissue. There was no significant reduction in the bioluminescence signal after injection of siScr-loaded hybrid micelles, indicating that the reduction in the bioluminescence intensity was due to the sequence-specific

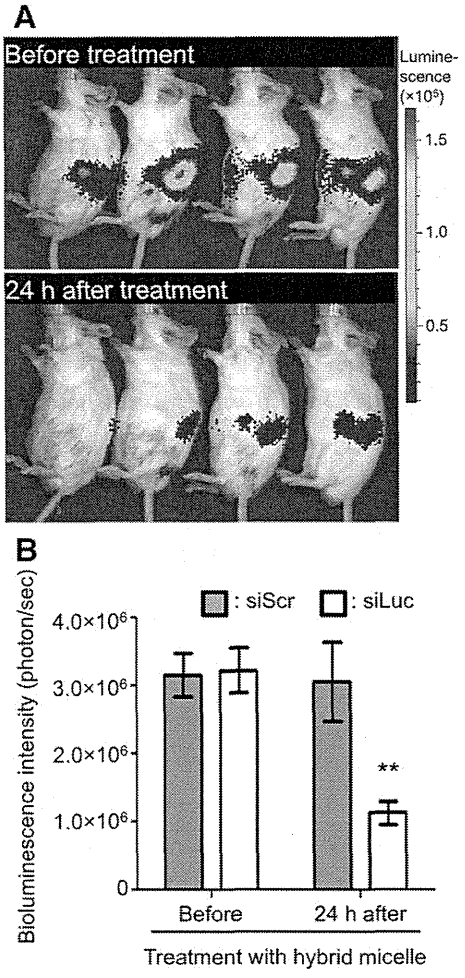

Fig. 6. *In vivo* gene silencing activity of systemically administered hybrid micelles in the spontaneous pancreatic tumors of transgenic mice. (A) Representative images of mice before and 24 h after injection of hybrid micelles containing siLuc (20 μg siRNA/mouse). (B) Bioluminescence intensity in the pancreatic tumors after intravenous injection of hybrid micelles containing siLuc or siScr (20 μg siRNA/mouse). Results are expressed as mean and standard deviation (n = 16). ANOVA followed by Newman–Keuls (**$P < 0.01$).

RNAi machinery. The similar gene silencing profile of hybrid micelles was further observed for the protein amount of luciferase in homogenized pancreas/tumor tissues (Supporting Fig. S2). This sequence-specific gene silencing activity of hybrid micelles is consistent with their significantly enhanced tumor accumulation of the siRNA payload (Figs. 4 and 5), which was roughly estimated to be ~1.3% of dose/g of tumor, corresponding to ~40 ng siRNA. Interestingly, the *in vivo* gene silencing efficacy of hybrid micelles in the spontaneous pancreatic cancer cells (60% with ~40 ng siRNA) was apparently higher than the *in vitro* efficacy in the cultured HeLa-Luc cells (50% with ~130 ng siRNA). These different efficacies might be due to varying cellular innate functions between the *in vivo* pancreatic cancer cells and the *in vitro* monolayer-cultured cervical cancer cells. The cellular innate functions, including the expression levels of luciferase and RNAi-related genes, are known to be substantially altered between live tissue and cell culture, especially monolayer culture, and also different types of cells [36–38]. Indeed, the luciferase expression in the present pancreatic cancer cells was lost in monolayer culture. This is the reason for the use of HeLa-Luc cells as a conventional cancer cell line for demonstrating the *in vitro* gene silencing activity of hybrid micelles.

3.5. Hematological parameters and cytokine levels after systemic administration of hybrid micelles

To verify the safety of the hybrid micelle formulation, hematological parameters and inflammatory cytokine levels were measured at several time points after systemic administration. As summarized in Table 1, the intravenous injection of hybrid micelles induced no remarkable changes in the levels of AST, ALT, and ALP as indicators of liver function and that of Cr as an indicator of kidney function over 48 h, suggesting negligible adverse side effects on the liver and the kidneys. Similarly, the levels of inflammatory cytokines, *i.e.*, TNF-α, IL-6, IL-1α, and IL-1β, were not affected by the injection of hybrid micelles (Supporting Fig. S3). Overall, it was demonstrated that the intravenous injection of hybrid micelles induced no severe acute toxicity under the tested conditions.

4. Conclusion

In the present study, hybrid micelles prepared with a smart block copolymer PEG-CCP were applied for systemic siRNA delivery to spontaneous pancreatic tumors in EL1-Luc/TAg transgenic mice. The obtained results confirmed the enhanced accumulation of siRNA-loaded hybrid micelles in the tumor tissue and their significant gene silencing activity. Notably, this was associated with negligible changes in hematological parameters. Altogether, the great potential of the hybrid micelles for RNAi-based cancer therapy was successfully demonstrated.

Acknowledgment

This research was funded by the Japan Society for the Promotion of Science (JSPS) through the "Funding Program for World-Leading Innovative R&D on Science and Technology (FIRST Program)," the Adaptable and Seamless Technology Transfer Program through Target-driven R&D (A-STEP), the National Institute of Biomedical Innovation (NIBIO), and Grants-in-Aid for Scientific Research from the Japanese Ministry of Health, Labour and Welfare. Part of this work was conducted in the Research Hub for Advanced Nano Characterization, The University of Tokyo, supported by the Ministry of Education, Culture, Sports, Science and Technology (MEXT), Japan. The authors are grateful to S. Ogura and K. Date for their assistance with animal care.

Appendix A. Supplementary data

Supplementary data to this article can be found online at http://dx.doi.org/10.1016/j.jconrel.2014.01.008.

References

[1] A. Fire, S. Xu, M.K. Montgomery, S.A. Kostas, S.E. Driver, C.C. Mello, Potent and specific genetic interference by double-stranded RNA in *Caenorhabditis elegans*, Nature 391 (1998) 806–811.

Table 1
Hematological parameters after intravenous injection of hybrid micelles (20 μg siRNA/mouse).

	Non-treated (0 min)	10 min	30 min	60 min	120 min	20 h	48 h
AST (U/L)	40 ± 5	38 ± 9	42 ± 4	40 ± 5	41 ± 5	36 ± 4	47 ± 7
ALT (U/L)	61 ± 18	62 ± 13	73 ± 5	67 ± 8	64 ± 12	86 ± 28	61 ± 23
ALP (U/L)	401 ± 25	401 ± 22	424 ± 10	378 ± 8	384 ± 23	377 ± 28	477 ± 37
Cr (mg/dL)	0.11 ± 0.01	0.11 ± 0.01	0.11 ± 0.01	0.10 ± 0.01	0.10 ± 0.01	0.10 ± 0.02	0.07 ± 0.01

Abbreviations: AST, aspartate aminotransferase; ALT, alanine aminotransferase; ALP, alkaline phosphatase; Cr, creatinine. Results are expressed as mean and standard deviation (n = 5).

[2] S.M. Elbashir, J. Harborth, W. Lendeckel, A. Yalcin, K. Weber, T. Tuschl, Duplexes of 21-nucleotide RNAs mediate RNA interference in cultured mammalian cells, Nature 411 (2001) 494–498.
[3] K. Whitehead, R. Langer, D. Anderson, Knocking down barriers: advances in siRNA delivery, Nat. Rev. Drug Discov. 8 (2009) 129–138.
[4] J.C. Burnett, J.J. Rossi, RNA-based therapeutics: current progress and future prospects, Chem. Biol. 19 (2012) 60–71.
[5] F. Takeshita, T. Ochiya, Therapeutic potential of RNA interference against cancer, Cancer Sci. 97 (2006) 689–696.
[6] Y.-K. Oh, T.G. Park, siRNA delivery systems for cancer treatment, Adv. Drug Deliv. Rev. 61 (2009) 850–862.
[7] F. van de Water, O. Boerman, A. Wouterse, J. Peters, F. Russel, R. Masereeuw, Intravenously administered short interfering RNA accumulates in the kidney and selectively suppresses gene function in renal proximal tubules, Drug Metab. Dispos. 34 (2006) 1393–1397.
[8] J. Turner, S. Jones, S. Moschos, M. Lindsay, M. Gait, MALDI-TOF mass spectral analysis of siRNA degradation in serum confirms an RNase A-like activity, Mol. Biosyst. 3 (2007) 43–50.
[9] R.J. Christie, N. Nishiyama, K. Kataoka, Delivering the code: polyplex carriers for deoxyribonucleic acid and ribonucleic acid interference therapies, Endocrinology 151 (2010) 466–473.
[10] C.A. Chen, H. Okayama, Calcium phosphate-mediated gene-transfer—a highly efficient transfection system for stably transforming cells with plasmid DNA, Biotechniques 6 (1988) 632.
[11] M. Jordan, A. Schallhorn, F.M. Wurm, Transfecting mammalian cells: optimization of critical parameters affecting calcium-phosphate precipitate formation, Nucleic Acids Res. 24 (1996) 596–601.
[12] Y. Kakizawa, K. Kataoka, Block copolymer self-assembly into monodispersive nanoparticles with hybrid core of antisense DNA and calcium phosphate, Langmuir 18 (2002) 4539–4543.
[13] M. Zhang, K. Kataoka, Nano-structured composites based on calcium phosphate for cellular delivery of therapeutic and diagnostic agents, Nano Today 4 (2009) 508–517.
[14] J. Li, Y.C. Chen, Y.C. Tseng, S. Mozumdar, L. Huang, Biodegradable calcium phosphate nanoparticle with lipid coating for systemic siRNA delivery, J. Control. Release 142 (2010) 416–421.
[15] Y. Kakizawa, K. Miyata, S. Furukawa, K. Kataoka, Size-controlled formation of a calcium phosphate-based organic–inorganic hybrid vector for gene delivery using poly(ethylene glycol)-block-poly(aspartic acid), Adv. Mater. 16 (2004) 699–702.
[16] Y. Kakizawa, S. Furukawa, K. Kataoka, Block copolymer-coated calcium phosphate nanoparticles sensing intracellular environment for oligodeoxynucleotide and siRNA delivery, J. Control. Release 97 (2004) 345–356.
[17] Y. Kakizawa, S. Furukawa, A. Ishii, K. Kataoka, Organic–inorganic hybrid-nanocarrier of siRNA constructing through the self-assembly of calcium phosphate and PEG-based block aniomer, J. Control. Release 111 (2006) 368–370.
[18] M. Zhang, A. Ishii, N. Nishiyama, S. Matsumoto, T. Ishii, Y. Yamasaki, K. Kataoka, PEGylated calcium phosphate nanocomposites as smart environment-sensitive carriers for siRNA delivery, Adv. Mater. 21 (2009) 3520–3525.
[19] F. Pittella, M. Zhang, Y. Lee, H.J. Kim, T. Tockary, K. Osada, T. Ishii, K. Miyata, N. Nishiyama, K. Kataoka, Enhanced endosomal escape of siRNA-incorporating hybrid nanoparticles from calcium phosphate and PEG-block charge-conversional polymer for efficient gene knockdown with negligible cytotoxicity, Biomaterials 32 (2011) 3106–3114.
[20] F. Pittella, K. Miyata, Y. Maeda, T. Suma, Q. Chen, R.J. Christie, K. Osada, N. Nishiyama, K. Kataoka, Pancreatic cancer therapy by systemic administration of VEGF siRNA contained in calcium phosphate/charge-conversional polymer hybrid nanoparticles, J. Control. Release 161 (2012) 868–874.
[21] H. Takemoto, K. Miyata, S. Hattori, T. Ishii, T. Suma, S. Uchida, N. Nishiyama, K. Kataoka, Acidic pH-responsive siRNA conjugate for reversible carrier stability and accelerated endosomal escape with reduced IFNα-associated immune response, Angew. Chem. Int. Ed. 52 (2013) 6218–6221.
[22] Y. Lee, K. Miyata, M. Oba, T. Ishii, S. Fukushima, M. Han, H. Koyama, N. Nishiyama, K. Kataoka, Charge conversion ternary polyplex with endosomes disruption moiety: a technique for efficient and safe gene delivery, Angew. Chem. Int. Ed. 120 (2008) 5241–5244.
[23] K.K. Frese, D.A. Tuveson, Maximizing mouse cancer models, Nat. Rev. Cancer 7 (2007) 654–658.
[24] G. Francia, W. Cruz-Munoz, S. Man, P. Xu, R.S. Kerbe, Mouse models of advanced spontaneous metastasis for experimental therapeutics, Nat. Rev. Cancer 11 (2011) 135–141.
[25] N. Zhang, S. Lyons, E. Lim, P. Lassota, A spontaneous acinar cell carcinoma model for monitoring progression of pancreatic lesions and response to treatment through noninvasive bioluminescence imaging, Clin. Cancer Res. 15 (2009) 4915–4924.
[26] K. Miyata, M. Oba, M. Nakanishi, S. Fukushima, Y. Yamasaki, H. Koyama, N. Nishiyama, K. Kataoka, Polyplexes from poly(aspartamide) bearing 1,2-diaminoethane side chains induce pH-selective, endosomal membrane destabilization with amplified transfection and negligible cytotoxicity, J. Am. Chem. Soc. 130 (2008) 16287–16294.
[27] K. Miyata, N. Nishiyama, K. Kataoka, Rational design of smart supramolecular assemblies for gene delivery: chemical challenges in the creation of artificial viruses, Chem. Soc. Rev. 41 (2012) 2562–2574.
[28] L.A. Aaltonen, S.R. Hamilton, World Health Organization; international agency for research on cancer, in: L.A. Aaltonen, S.R. Hamilton (Eds.), Pathology and Genetics of Tumours of the Digestive System, IARC Press: Oxford University Press, Lyon: Oxford, 2000, (314 pp.).
[29] R.A. Caruso, A. Inferrera, G. Tuccari, G. Barresi, Acinar cell carcinoma of the pancreas, a histologic, immunocytochemical and ultrastructural study, Histol. Histopathol. 9 (1994) 53–58.
[30] H. Cabral, M. Murakami, H. Hojo, Y. Terada, M.R. Kano, U.-I. Chung, N. Nishiyama, K. Kataoka, Targeted therapy of spontaneous murine pancreatic tumors by polymeric micelles prolongs survival and prevents peritoneal metastasis, Proc. Natl. Acad. Sci. U. S. A. 110 (2013) 11397–11402.
[31] M.R. Kano, Y. Bae, C. Iwata, Y. Morishita, M. Yashiro, M. Oka, T. Fujii, A. Komuro, K. Kiyono, M. Kaminishi, K. Hirakawa, Y. Ouchi, N. Nishiyama, K. Kataoka, K. Miyazono, Improvement of cancer-targeting therapy, using nanocarriers for intractable solid tumors by inhibition of TGF-β signaling, Proc. Natl. Acad. Sci. U. S. A. 104 (2007) 3460–3465.
[32] L. Zhang, H. Nishihara, M.R. Kano, Pericyte-coverage of human tumor vasculature and nanoparticle permeability, Biol. Pharm. Bull. 35 (2012) 761–766.
[33] H. Cabral, Y. Matsumoto, K. Mizuno, Q. Chen, M. Murakami, M. Kimura, Y. Terada, M.R. Kano, K. Miyazono, M. Uesaka, N. Nishiyama, K. Kataoka, Accumulation of sub-100 nm polymeric micelles in poorly permeable tumours depends on size, Nat. Nanotechnol. 6 (2011) 815–823.
[34] American Cancer Society, Cancer Facts & Figs. 2011, Epidemiologic Surveillance Report, American Cancer Society, Atlanta, 2011, (available at: <http://www.cancer.org/acs/groups/content/@epidemiologysurveilance/documents/document/acspc-029771.pdf>. Accessed April 2013).
[35] A. Jemal, R. Siegel, J. Xu, E. Ward, Cancer statistics, 2010, CA Cancer J. Clin. 260 (2010) 277–300.
[36] F. Pampaloni, E.G. Reynaud, E.H.K. Stelzer, The third dimension bridges the gap between cell culture and live tissue, Nat. Rev. Mol. Cell Biol. 8 (2007) 839–845.
[37] N.J. Yoo, S.Y. Hur, M.S. Kim, J.Y. Lee, S.H. Lee, Immunohistochemical analysis of RNA-induced silencing complex-related proteins AGO2 and TNRC6A in prostate and esophageal cancers, APMIS 118 (2010) 271–276.
[38] T. Endo, K. Itaka, M. Shioyama, S. Uchida, K. Kataoka, Gene transfection to spheroid culture system on micropatterned culture plate by polyplex nanomicelle: a novel platform of genetically-modified cell transplantation, Drug Deliv. Transl. Res. 2 (2012) 398–405.

JACS
JOURNAL OF THE AMERICAN CHEMICAL SOCIETY
Article
pubs.acs.org/JACS

Phenylboronic Acid-Installed Polymeric Micelles for Targeting Sialylated Epitopes in Solid Tumors

Stephanie Deshayes,[†,◆] Horacio Cabral,[‡,◆] Takehiko Ishii,[‡] Yutaka Miura,[§,∥] Shutaro Kobayashi,[†] Takashi Yamashita,[⊥] Akira Matsumoto,[#] Yuji Miyahara,[#] Nobuhiro Nishiyama,[○] and Kazunori Kataoka*[,†,‡,∥,▽]

[†]Department of Materials Engineering, [‡]Department of Bioengineering, [§]Division of Tissue Engineering, and [∥]Center for Disease Biology and Integrative Medicine, Graduate School of Engineering, The University of Tokyo, 7-3-1 Hongo, Bunkyo-ku, Tokyo 113-8656, Japan

[⊥]Department of Pure and Applied Chemistry, Graduate School of Science and Technology, Tokyo University of Science, 2641 Yamazaki, Noda-shi, Chiba-ken 278-8510, Japan

[#]Institute of Biomaterials and Bioengineering, Tokyo Medical and Dental University, 2-3-10 Kanda-Surugadai, TokyoChiyoda-ku, 101-0062, Japan

[○]Polymer Chemistry Division, Chemical Resources Laboratory, Tokyo Institute of Technology, R1-11, 4259 Nagatsuta, Midori-ku, Yokohama 226-8503, Japan

[▽]Center for NanoBio Integration, The University of Tokyo, 7-3-1 Hongo, Bunkyo-ku, Tokyo 113-8656, Japan

Supporting Information

ABSTRACT: Ligand-mediated targeting of nanocarriers to tumors is an attractive strategy for increasing the efficiency of chemotherapies. Sialylated glycans represent a propitious target as they are broadly overexpressed in tumor cells. Because phenylboronic acid (PBA) can selectively recognize sialic acid (SA), herein, we developed PBA-installed micellar nanocarriers incorporating the parent complex of the anticancer drug oxaliplatin, for targeting sialylated epitopes overexpressed on cancer cells. Following PBA-installation, the micelles showed high affinity for SA, as confirmed by fluorescence spectroscopy even at intratumoral pH conditions, i.e., pH 6.5, improving their cellular recognition and uptake and enhancing their *in vitro* cytotoxicity against B16F10 murine melanoma cells. *In vivo*, PBA-installed micelles effectively reduced the growth rate of both orthotopic and lung metastasis models of melanoma, suggesting the potential of PBA-installed nanocarriers for enhanced tumor targeting

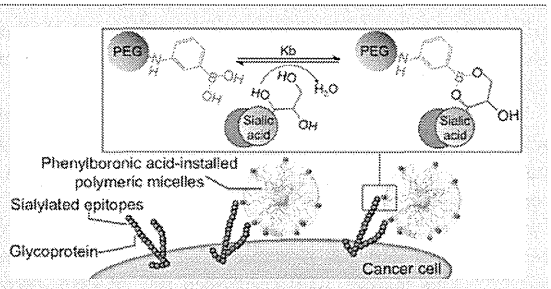

INTRODUCTION

Nanocarriers have shown great potential for selectively delivering high payloads of therapeutic molecules to tumors.[1−5] When systemically injected, long-circulating nanocarriers can specifically accumulate in solid tumors due to the increased permeability of the tumor vasculature and be retained because of the impaired lymphatic drainage at the cancerous site.[6] By functionalization of the surface of these nanocarriers with ligands capable of recognition of cell-specific surface receptors, they can be rendered with cellular selectivity and superior intracellular delivery.[2,3,7−12] Thus, antibodies,[8] antibody fragments,[9] aptamers,[10] peptides,[11,12] and small molecules[13] have been used as ligands for improving the tumor targeting ability of nanocarriers. The efficiency of ligand-installed nanocarriers for targeting cancer cells is affected by several features, such as the binding affinity of the ligands to the receptors, the rate of internalization, the density and availability of the receptors, the intratumoral distribution of the receptors and the variation of the receptor expression with the tumor stage.[7−13] Therefore, effective approaches for ligand-mediated targeting of nanocarriers require suitable recognition of the versatile receptor landscapes of tumors.

Carbohydrate antigens, which are expressed in all tumor cells due to aberrant glycosylation[14−16] represent an exceptional target for ligand-mediated targeting of nanocarriers, as they are displayed in tumors more frequently than oncogene markers, such as HER2/neu.[15] These malignant glycophenotypes overexpress sialylated epitopes, i.e., glycan chains containing *N*-acetylneuraminic acid (Neu5Ac), which is the predominant sialic acid (SA) in humans.[14−16] The increased expression of sialylated antigens on cancer cells is closely related with cancer progression and with poor prognosis in patients with lung, breast, colon, prostate, bladder, and stomach cancer.[14−16] Moreover, hypoxic regions of solid tumors have shown increased levels of sialylated antigens,[17] and the overexpression of sialylated glycans, such as Sialyl-Lewis^x and Sialyl-Lewis^a, is important for the formation of metastases.[18] SA has been

Received: June 24, 2013
Published: September 12, 2013

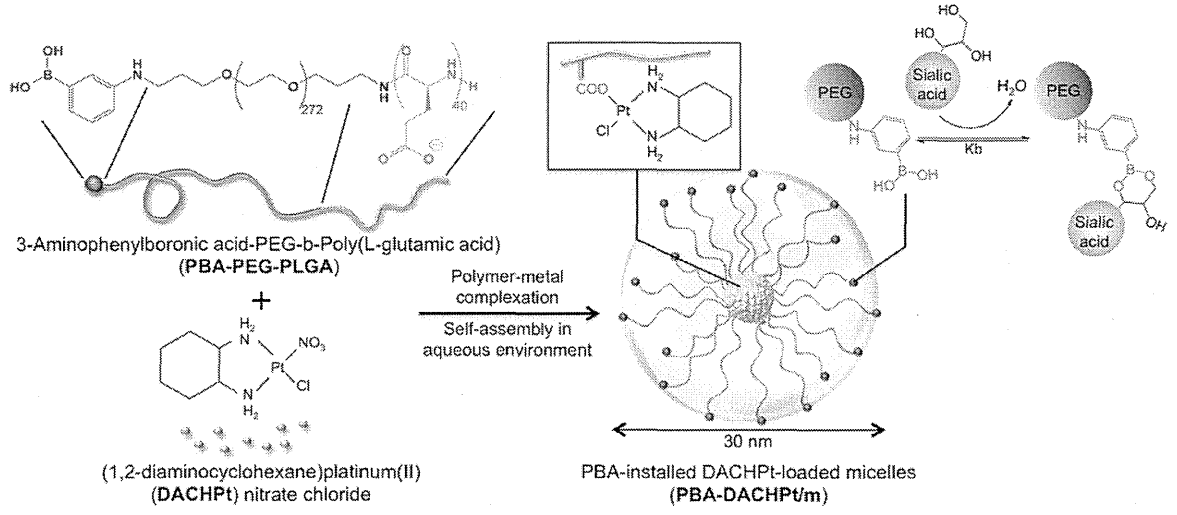

Figure 1. Preparation of PBA-installed DACHPt-loaded micelles by self-assembly through polymer–metal complex formation between DACHPt and PBA-poly(ethylene glycol)-*b*-poly(L-glutamic acid) in distilled water. PBA moieties on the surface of the micelles can bind to SA.

targeted *in vitro* by using lectin[19] and antibodies,[20] such as the tumoral marker CA19-9, used for detection of Sialyl-Lewis[a] in gastrointestinal tumors. Nevertheless, these approaches have been difficult to translate *in vivo*, mainly because of their immunogenicity. Moreover, as SA is also present on red blood cells and the luminal surfaces of vascular endothelium,[21,22] systemically injected ligands for SA targeting should not be active until reaching the site of tumors.

We have recently demonstrated the ability of phenylboronic acid (PBA) for selective recognition of SA overexpressed on the surface of cancer cells.[23] Although PBA can also form complexes with other common sugars, they are unstable unless formed at pHs higher than its pK_a value, whereas the complex between PBA and SA is stable even at pHs lower than its pK_a.[24,25] This feature, with controlled pK_a of PBA, provides a molecular basis for the specific SA recognition at physiological pH. This interaction has been recently used for determining the sialylation status of solid tumors by MRI through PBA-based reporters.[26] In addition to the high affinity and selectivity for SA, PBA presents several advantages for targeting of cancer cells such as being nontoxic, nonimmunogenic, and inexpensive.

Herein, we developed PBA-functionalized nanocarriers by installing PBA moieties on the polymeric micelles for specific targeting of SA epitopes overexpressed on tumor cells. Polymeric micelles, i.e., core–shell self-assemblies of block copolymers, provide multiple advantages as nanocarriers including their nanoscaled size, their poly(ethylene glycol) (PEG) shell, which prevents their recognition by macrophages of the reticuloendothelial system (RES) and prolongs their blood circulation time, and hydrophobic core for loading and controlled release of bioactive molecules.[4,5,27–29] Our polymeric micelles incorporating the anticancer drugs paclitaxel, SN-38, cisplatin, and the parent complex of oxaliplatin, i.e., dichloro(1,2-diamino-cyclohexane)platinum(II) (DACHPt), have advanced to clinical studies,[30,31] demonstrating high efficacy against several intractable tumors, such as triple-negative breast cancers, and less side effects in patients.[30] In this study, we use DACHPt-loaded micelles (DACHPt/m), which have shown selective accumulation in tumor tissues and strong suppression of the growth of several tumor models,[32–35] to prepare polymeric micelles having PBA moieties on their surface. The micelles were self-assembled through the coordination bond between platinum drug and the carboxylic groups of PBA-poly(ethylene glycol)-*b*-poly(L-glutamic acid) [PBA-PEG-*b*-PLGA] copolymers in water (Figure 1). The inherent fluorescence of PBA installed to PEG-*b*-PLGA copolymers was used for studying its binding affinity against different sugars by fluorescence spectroscopy. Moreover, the ability of PBA-installed DACHPt/m (PBA-DACHPt/m) to target SA in tumors was evaluated *in vitro* as well as *in vivo* against orthotopic and metastatic tumor models. For this purpose, highly metastatic B16F10 murine melanoma cells overexpressing SA on their surface[36] were used, for which we have recently established a method of quantification based on the PBA-SA interaction.[23] Our results showed a high selectivity of PBA-DACHPt/m to SA epitopes, which enhanced their cellular uptake *in vitro* and improved their tumor accumulation and retention *in vivo*, leading to a superior antitumor effect.

■ RESULTS AND DISCUSSION

Preparation of PBA End-Functionalized PEG-*b*-PLGA. Acetal-poly(ethylene glycol)-*b*-poly(L-glutamic acid) [acetal-PEG-*b*-PLGA] block copolymer was reacted with 3-aminophenylboronic acid by one pot reductive amination to afford aminophenylboronic acid-poly(ethylene glycol)-*b*-poly(L-glutamic acid) [PBA-PEG-*b*-PLGA] copolymer (Scheme S1). Thus, after deprotection of the acetal residue under acidic conditions, the obtained aldehyde group formed a Schiff base with 3-amino-substituted PBA. This intermediate imine was reduced to a secondary amine by using $NaBH_3CN$. The PBA installation at PEG end was confirmed to be almost quantitative by the proton ratios of the aromatic group of PBA and the ethylene units in PEG in the ^1H NMR spectrum (Figure S1).

Binding Affinities of PBA-PEG-*b*-PLGA to Various Sugars. Most sugars can complex only with the tetrahedral anionic form of boronate, because the complex with the trigonal neutral form is usually susceptible to hydrolysis.[37] In contrast, SA-PBA complexation is also favored by the trigonal form, for which involvement of multiple metastable binding sites along with intramolecular stabilization via B–N or B–O interactions are likely to play roles.[24,38,39] The pK_a value of the

polymer conjugated PBA, as assessed by fluorescence titration (Figure S2), was determined to be 9.7. This value, which is safely higher than that of physiological conditions, indicates predominant fraction of trigonal (undissociated) PBA at pH 7.4 and, thus, warrants specificity to SA.

To demonstrate the specificity of the PBA modified polymer for SA, we evaluated the binding affinities of PBA-PEG-*b*-PLGA for a series of sugars, such as glucose, mannose, galactose, Neu5Ac, and 2-O-methyl-α-D-*N*-acetylneuraminic acid (Me-Neu5Ac; Me-SA), which is a model for neuraminic residues present in the terminal positions of glycan chains,[40] by steady-state fluorescence quenching measurements. While the complexation of sugars has been reported to alter the fluorescence of boron-containing fluorophores,[41,42] in this study, we took advantage of the intrinsic fluorescence property of PBA-PEG-*b*-PLGA. The fluorescence property of PBA was maintained after PBA conjugation to the polymer end (Figure 2A). Moreover, because the binding of PBA to sugars is affected by pH,[37] we perform the experiments at pH 7.4, i.e., physiological pH, and at pH 6.5, which is the lowest environmental pH found inside tumors.[43] The fluorescence spectra of PBA-PEG-*b*-PLGA were collected in the presence of glucose, galactose, mannose, or Neu5Ac. Figure 2B shows the representative fluorescence spectra of PBA-PEG-*b*-PLGA on addition of Neu5Ac at pH 7.4, illustrating a quenching of fluorescence to occur due to photoinduced electron transfer (PET) as a result of the PBA-Neu5Ac complexation.[44,45] Accordingly, the relative fluorescence intensities of PBA-PEG-*b*-PLGA as a function of sugar concentration at pH 7.4 are shown in Figure 2C and at pH 6.5 in Figure 2D. The kinetic of the fluorescence quenching follows the Stern–Volmer equation (eq 1):

$$I_0/I = 1 + K_b\cdot[Q] = 1 + k_q''\cdot\tau_0\cdot[Q] \quad (1)$$

where I_0 represents the initial fluorescence intensity of the PBA-PEG-*b*-PLGA without sugar, I is the fluorescence intensity of the PBA-PEG-*b*-PLGA in the presence of the sugar (quencher), K_b is the binding constant (M^{-1}), k_q is the quencher rate coefficient ($M^{-1}s^{-1}$), τ_0 is the fluorescence lifetime of PBA-PEG-*b*-PLGA without quencher, and [Q] is the concentration of the quencher.

The binding constants are given as a slope in the Stern–Volmer plot (Figure 2C,D) and reported in Table 1.

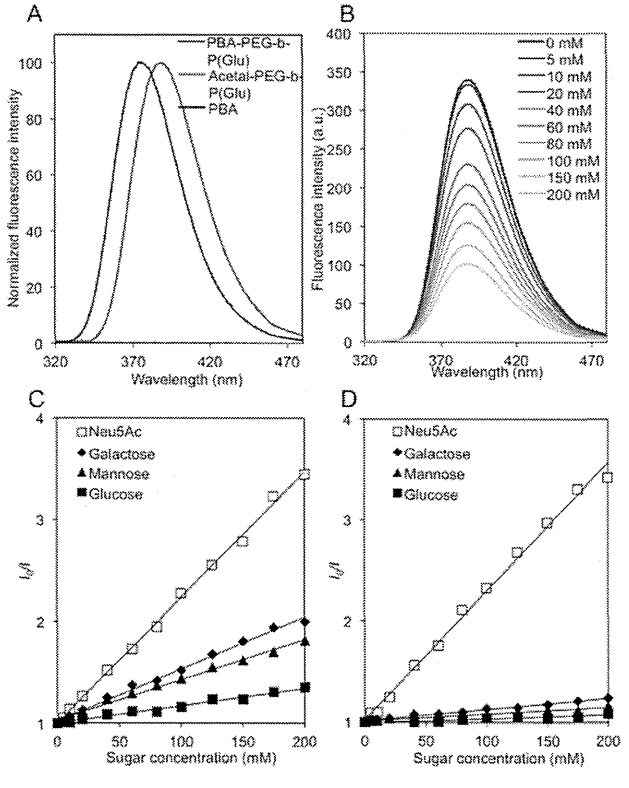

Figure 2. (A) Emission spectra of PBA, Acetal-PEG-*b*-PLGA and PBA-PEG-*b*-PLGA in phosphate buffer (0.1 M, pH 7.4) at room temperature, λ_{ex} = 302 nm. B. Emission spectra of PBA-PEG-*b*-PLGA (40 μM) in phosphate buffer solution (0.1 M, pH 7.4) containing various concentrations of Neu5Ac (0–200 mM) at room temperature, λ_{ex} = 302 nm. Relative fluorescence as a function of sugar concentration for PBA-PEG-*b*-PLGA measured in phosphate buffer (0.1 M) at room temperature (λ_{ex} = 302 nm and λ_{em} = 388 nm) at pH 7.4 (C) and pH 6.5 (D). I_0 and I represent the fluorescence intensity in the absence and presence of sugar respectively. Data were fit according to Stern–Volmer equation (eq 1).

Table 1. Binding Constants and Rate Coefficients of PBA-PEG-*b*-PLGA and Sugars in Phosphate Buffer pH 7.4 and 6.5[a]

		pH		
sugar		7.4	6.5	K_b 6.5/ K_b 7.4
glucose	K_b (M^{-1})	1.71	0.39	0.29
	$k_q \times 10^{-9}$ ($M^{-1}\cdot s^{-1}$)	0.18	0.04	–
mannose	K_b (M^{-1})	3.95	0.70	0.17
	$k_q \times 10^{-9}$ ($M^{-1}\cdot s^{-1}$)	0.41	0.07	–
galactose	K_b (M^{-1})	5.11	1.11	0.21
	$k_q \times 10^{-9}$ ($M^{-1}\cdot s^{-1}$)	0.53	0.11	–
NeuSAc (SA)	K_b (M^{-1})	12.3	12.7	1.03
	$k_q \times 10^{-9}$ ($M^{-1}\cdot s^{-1}$)	1.28	1.32	–
MeNeuSAc (Me-SA)	K_b (M^{-1})	3.40	6.00	1.76
	$k_q \times 10^{-9}$ ($M^{-1}\cdot s^{-1}$)	0.35	0.62	–

[a]Determined by steady-state fluorescence quenching measurements; τ_0 (ns) at pH 7.4 was 9.62 ± 49.2 and at pH 6.5 was 9.67 ± 49.2.

Furthermore, the quencher rate coefficients were assessed from the fluorescence lifetimes (Table 1), which remained unchanged for these pHs (6.5 and 7.4). We observed that the binding constants and the quencher rate coefficients were remarkably higher for Neu5Ac than those for other sugars, indicating a stronger affinity for SA. The binding constant values showed similar tendency with previously reported values using other boronic acids and different methods (UV,[46] ^{11}B-NMR,[24] or indirect fluorescence through the fluorescent reporter compound, Alizarin Red S[47]). Moreover, even though the affinity for sugars depends on the nature of boronic acid, a trend for the selectivity was noticed as SA ≫ galactose ≥ mannose ≅ glucose. It is worth noticing that the ratio between the binding constant at intratumoral pH, i.e., K_b 6.5, and that for pH 7.4, i.e., K_b 7.4, is maintained close to 1 for Neu5Ac, while it is <1 for others (Table 1), suggesting a higher binding efficiency of PBA for SA in the intratumoral environment. Moreover, the presence of a methyl group at the C2 hydroxyl

dx.doi.org/10.1021/ja406406h | J. Am. Chem. Soc. 2013, 135, 15501–15507

group of Me-SA reduced the binding constant, K_b, from 12.3 M^{-1} for SA to 3.4 M^{-1} for MeSA at pH 7.4 (Table 1). At pH 6.5, even though K_b decreased from 12.7 M^{-1} for SA to 6 M^{-1} for Me-SA, this binding constant was higher than the binding constants for the other sugars, indicating the selectivity of PBA for biological relevant SA at intratumoral pH (Table 1). Moreover, as K_b for Me-SA is higher at intratumoral pH than at physiological pH, it is expected that while the complex between PBA and SA will compete with other sugars in the bloodstream (pH 7.4), the PBA-installed micelles would primarily target SA under increasingly acidic conditions relevant to the environment of tumors.

Preparation and Characterization of PBA-Installed DACHPt-Loaded Micelles. Micelles were self-assembled due to the metal–polymer complexation between the carboxylic group of the PLGA and the platinum of DACHPt (Figure 1). Dynamic light scattering (DLS) measurements showed that the diameters of DACHPt/m and PBA-DACHPt/m were comparable, i.e., ~30 nm by weight distribution (Figure 3 and Table 2). Accordingly, these diameters may be suitable for achieving deep penetration in solid tumors, as we have recently demonstrated that 30 nm DACHPt/m can deeply penetrate even in poorly permeable malignancies.[35] Both micelles also showed comparable ζ potential values, which were slightly negative at pH 7.4 (Table 2). The Pt content in both micelles was found to be similar and remarkably high (Table 2), as determined by inductively coupled plasma mass spectrometry (ICP-MS). Moreover, in media containing chloride ions, i.e., 10 mM PBS plus 150 mM NaCl, DACHPt is released from the core of the micelles by exchange reaction between chloride ions and carboxylic groups of PLGA.[32−34] Accordingly, the conjugation of PBA ligands did not affect the drug release rate of the micelles, and both DACHPt/m and PBA-DACHPt/m released ~40% of DACHPt after 2 days (Figure S3), which is similar to our previous reports.[32−34]

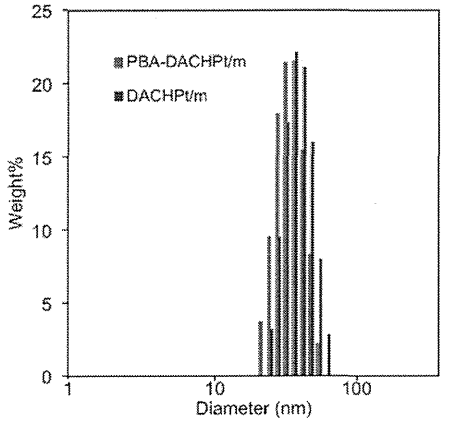

Figure 3. Diameter of DACHPt/m and PBA-DACHPt/m by weight distribution determined by DLS.

Table 2. Diameter, Polydispersity, Drug Loading and ζ Potential of DACHPt/m and PBA-DACHPt/m

	DACHPt/m	PBA-DACHPt/m
diameter[a] (nm)	35	29
polydispersity index[a]	0.1	0.1
ζ potential (mV)[b]	−2.3 ± 1.4	−5.7 ± 0.3
Pt/polymer (wt/wt %)[c]	30	31
[Pt]/[COO] (mol/mol %)[c]	50	52

[a]Determined by weight% distribution obtained with DLS. [b]Determined in 10 mM phosphate buffer, pH 7.4. [c]Determined by ICP-MS.

***In vitro* Targeting Ability of PBA-Installed DACHPt-Loaded Micelles.** The ability of PBA-DACHPt/m to bind SA epitopes in cancer cells was studied *in vitro*. First, we evaluated the cellular uptake of fluorescent-labeled micelles in B16F10 murine melanoma cells, which overexpress SA on the membrane,[23,36] by confocal laser microscopy. For constructing the fluorescent-labeled micelles, we conjugated Alexa Fluor 555 succinimidyl ester to the ω-amino group of MeO-PEG-*b*-PLGA and PBA-PEG-*b*-PLGA and obtained MeO-PEG-*b*-PLGA-$Alexa_{555}$ and PBA-PEG-*b*-PLGA-$Alexa_{555}$. The conjugation degree of Alexa Fluor 555 was 4 mol % for both polymers. We built the fluorescent micelles following the same method as for unlabeled micelles. After micelle formation, the fluorescence signal from the Alexa Fluor 555 probes in the core of the micelles was still detectable. Thus, after incubating the cells with the fluorescent micelles for 3 h, the fluorescent signal of PBA-DACHPt/m was significantly higher than that of DACHPt/m, indicating a faster cellular uptake (Figure 4A,B). After 6 h incubation, the difference between the micelles became more evident, as the fluorescent signal from PBA-DACHPt/m was localized inside the cells, while the signal from DACHPt/m was barely detectable (Figure 4A,B). After 9 h incubation, even though the fluorescent DACHPt/m was detected inside the tumor cells due to nonspecific uptake (Figure 4A,B), the fluorescent signal of PBA-DACHPt/m was still significantly higher (Figure 4B; $p < 0.001$). The addition of free PBA to the cell culture media reduced the cellular uptake of PBA-DACHPt/m, which showed a similar intensity to DACHPt/m (Figure 4A,B), indicating that the enhanced cellular uptake of PBA-DACHPt/m is due to the interaction of PBA moieties with the cells. Furthermore, treating the cells with sialidase, which is an enzyme that can cleave SA epitopes from the cells, before incubation with the micelles, led to a drastic decrease of the cellular internalization of PBA-DACHPt/m (Figure 4A,B), demonstrating the specific interaction of these micelles with SA epitopes on the cell membrane. For both free PBA- and sialidase-treated cells, the intracellular signal of fluorescent-labeled PBA-DACHPt micelles increased after 9 h incubation, comparable to nontargeted DACHPt/m with fluorescent-labeling, probably due to nonspecific uptake.

The enhancement of the antitumor effect of PBA-installed micelles was determined by evaluating the 50% growth inhibitory concentration (IC_{50}) against B16F10 cells. Moreover, the activity of the micelles was compared with that of oxaliplatin, because it is the clinically approved DACHPt-derivative and presents the same active complexes as the micelles. After exposing the cells to oxaliplatin or micelles for 3 h, the cells were washed and postincubated for 48 h. Thus, while free oxaliplatin showed lower IC_{50} than both micelles, probably due to its rapid cellular internalization as well as the slow sustained release of DACHPt complexes from the micelles, the cytotoxicity of PBA-DACHPt/m was higher than that of DACHPt/m (Table 3), which correlated with the increased cellular uptake of these micelles, suggesting their potential for enhancing the therapeutic effect *in vivo*.

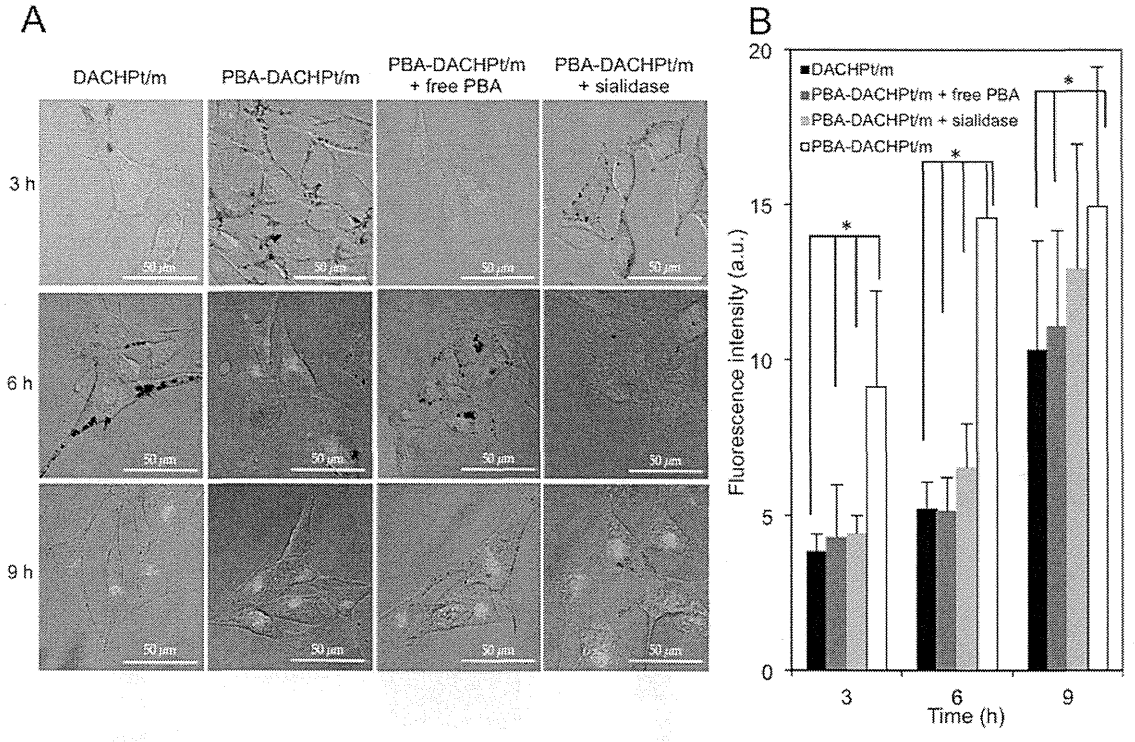

Figure 4. (A) Fluorescent microscopies of B16F10 cells incubated with fluorescent-labeled DACHPt/m or PBA- DACHPt/m for 3, 6, and 9 h. Free PBA was added 10 min before the addition of PBA- DACHPt/m for the competition assay. To cleave specifically SA, the cells were pretreated with sialidase before the incubation with PBA-DACHPt/m. The polymers were labeled with a fluorescent dye (Alexa Fluor 555; red). (B) Quantification of the fluorescence intensity. Data are expressed as averages ± S.E.M., $n = 20$, $^*p < 0.001$.

Table 3. *In vitro* Cytotoxicity of Free Oxaliplatin, DACHPt/m, and PBA-DACHPt/m after 48 h of Total Incubation Against B16F10 Cell Line

	IC_{50} (μM)[a]		
cells	oxaliplatin	DACHPt/m	PBA-DACHPt/m
B16F10	142 ± 5	278 ± 11	184 ± 8

[a]Determined by WST-8 assay ($n = 8$).

***In vivo* Targeting Ability of PBA-Installed DACHPt-Loaded Micelles.** The performance of the micelles was evaluated *in vivo* in mice bearing B16F10 melanoma tumors. Accordingly, intravenously injected DACHPt/m and PBA-DACHPt/m showed similar prolonged blood circulation with ~20% of injected dose per ml of plasma after 24 h (Figure 5A), which is in agreement with our previous results for DACHPt/m,[32,34,35] suggesting the reduced interaction of PBA-DACHPt/m with red blood cells and endothelial cells in the vasculature. This reduced interaction may be due to the interference by glucose in plasma, as normal glucose levels are ~5 mM, while the concentration of SA in erythrocytes (SA_{RBC}) is ~0.2 μM (20 nmol/10^9 cells).[48] Conversely, inside tumors, the glucose concentration decreases due to diffusion and the persistent metabolism of glucose to lactate in cancer cells.[49] Moreover, the metabolic products of this anaerobic glycolysis cause acidification of the intratumoral space, which decreases the binding constant for glucose (Table 1). Because the binding constant for SA at intratumoral pH is maintained and the SA amount on B16F10 cells is 1.1 nmol/10^6 cells,[23] which is more than 1000-fold higher than for erythrocytes, we expect that PBA-DACHPt/m effectively bind to tumor cells *in vivo*.

The tumor accumulation of DACHPt/m and PBA-DACHPt/m was similar up to 24 h, reaching ~5% of the injected dose per g of tissue. However, 48 h after injection, the amount of DACHPt/m in the tumors declined, whereas PBA-DACHPt/m maintained their accumulation level in the tumor (Figure 5B; $p < 0.05$), suggesting that the interaction of PBA-DACHPt/m with the SA moieties on the surface of cancer cells improved the retention of micelles at the tumor site. As this prolonged tumor retention increases the exposure of the cancer cells to anticancer drugs, it may enhance the antitumor activity of PBA-DACHPt/m.

The antitumor activity of PBA-DACHPt/m was evaluated in an orthotopic tumor model prepared by intradermal inoculation of B16F10 cells to mice ($n = 5$). Mice were treated with intravenous injection three times at 2 day intervals, i.e., at days 0, 2, and 4, with oxaliplatin at dose of 8 mg/kg, and DACHPt/m or PBA-DACHPt/m at a dose of 3 mg/kg. These doses were selected based on our previous observations for the maximum tolerated dose for oxaliplatin and the effective dose for DACHPt/m.[33] Thus, while free oxaliplatin failed to show any antitumor effect, probably due to its low accumulation in tumor tissues as well as its inactivation due to binding to serum proteins and erythrocytes after systemic administration,[50] both DACHPt/m and PBA-DACHPt/m significantly reduced the growth rate of the tumors, correlating with their enhanced accumulation in tumors (Figure 5B),with PBA-DACHPt/m showing higher efficacy than DACHPt/m ($p = 0.005$) (Figure 5C). Moreover, polymeric micelles can protect the Pt drug in their core during circulation and enhance the drug delivery to the nucleus of cancer cells,[34] therefore, increasing the *in vivo* antitumor efficacy of the Pt drug. In addition, this activity

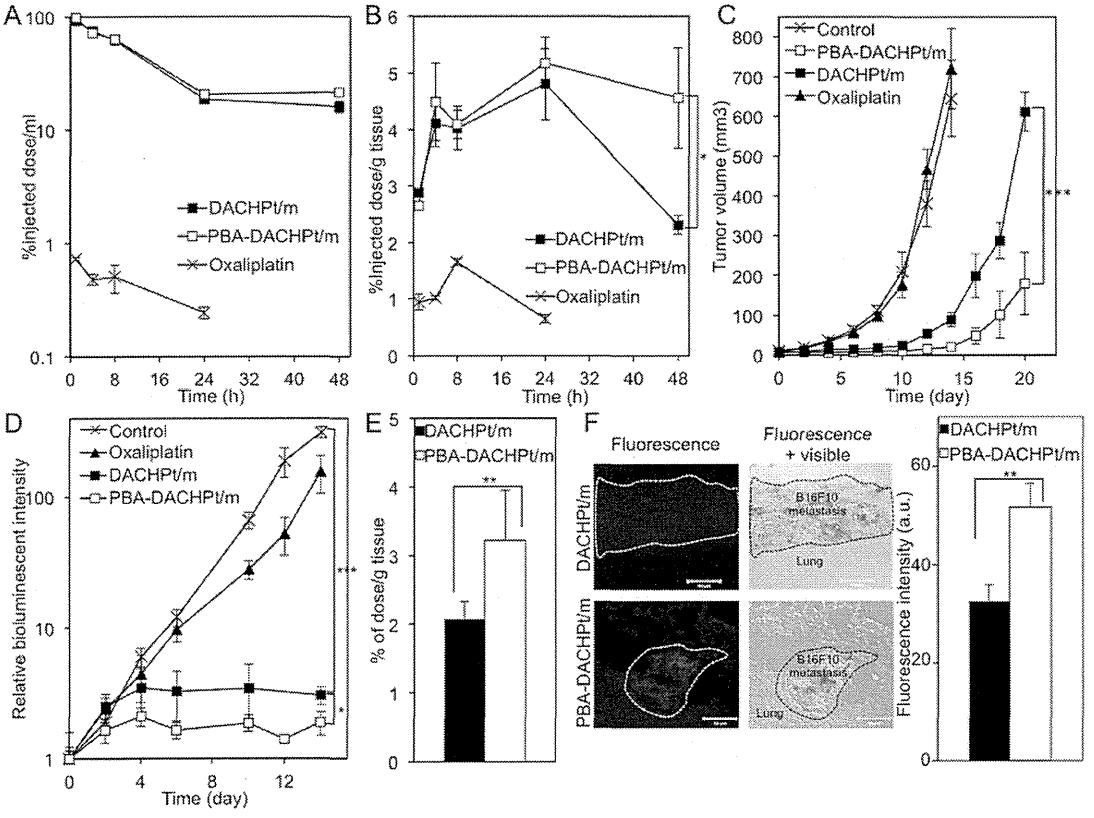

Figure 5. *In vivo* properties of PBA-DACHPt/m. (A) Plasma clearance and (B) tumor accumulation of DACHPt/m and PBA-DACHPt/m in mice bearing B16F10 tumor model. Data are means ± S.E.M.; $n = 5$; $^{*}p < 0.05$. (C) Antitumor activity against orthotopic B16F10 tumors after treatment with oxaliplatin (8 mg/kg), DACHPt/m or PBA-DACHPt/m (3 mg/kg) injected on days 0, 2, and 4. Data are expressed as averages ± S.E.M.; $n = 5$; $^{***}p < 0.001$. (D) Antitumor activity against lung metastasis induced by B16F10-Luc melanoma cells. Data are expressed as averages ± S.E.M.; $n = 5$; $^{*}p < 0.05$; $^{***}p < 0.001$. (E) Accumulation of micelles in lungs having B16F10-Luc melanoma cells 24 h after the intravenous injection. Data are expressed as averages ± S.E.M., $n = 6$, $^{**}p < 0.005$. (F) Ex vivo fluorescent microscopies of lung tissues bearing B16F10-Luc metastasis 24 h after the injection of fluorescent-labeled DACHPt/m or PBA-DACHPt/m (Alexa Fluor 647; pink) and quantification of fluorescent intensity in metastatic regions. Data are expressed as averages ± S.E.M., $n = 3$, $^{**}p < 0.005$.

enhancement did not come at the expense of side effects, and the body weight of the mice remained stable even after the repeated administration of the micelles (Figure S4).

In addition, as metastasis is the major cause of cancer-related death and because the expression of SA is highly associated with the metastatic disease,[18] we evaluated the efficiency of PBA-DACHPt/m against bioluminescent lung metastasis, obtained after intravenous injection of B16F10 cells expressing luciferase (B16F10-Luc) in BALB/c nu/nu mice. Mice were treated intravenously three times at 2 day intervals, i.e., at days 0, 2, and 4, with oxaliplatin at dose of 8 mg/kg, DACHPt/m or PBA-DACHPt/m at a dose of 3 mg/kg. By following the growth of metastasis through imaging the bioluminescence signal, we observed that, while oxaliplatin showed no antitumor effect (Figure 5D), both DACHPt/m and PBA-DACHPt/m significantly inhibited the progression of the metastasis. Again, PBA-DACHPt/m demonstrated to be more efficacious than DACHPt/m, showing 2-fold lower bioluminescent intensity (Figure 5D; $p < 0.05$). The enhanced activity of PBA-DACHPt/m matched the increased Pt accumulation of these micelles in metastatic lungs 24 h after injection (Figure 5E). Moreover, the specificity of PBA-DACHPt/m to the metastatic sites in lungs was confirmed by histology after the injection of micelles labeled with Alexa Fluor 647 (Figure 5F). Thus, the fluorescence intensity for PBA-DACHPt/m was higher than that for DACHPt/m at the metastatic regions, supporting the superior efficacy of PBA-DACHPt/m.

■ CONCLUSION

Our findings demonstrated that PBA conjugation of the surface of polymeric micellar nanocarriers enhanced their tumor targeting ability, by specific interaction with SA epitopes overexpressed in tumor cells, without affecting their long circulating properties. These results support the application of borate ester chemistry for specific targeting of tumor-associated carbohydrate antigens at intratumoral pH conditions. Moreover, because of the clear relationship between overexpression of sialylated epitopes, tumor aggressiveness, and patients' prognosis as well as the safety and nonimmunogenicity of the approach, PBA-mediated targeting of nanocarriers offers a highly translational approach for clinical diagnosis and therapy of solid tumors.

■ ASSOCIATED CONTENT

Ⓢ Supporting Information

Experimental section, preparation scheme, and ^{1}H NMR of PBA-PEG-*b*-PLGA, study of the pK_a of PBA-PEG-*b*-PLGA, the release rate profiles of the micelles and their *in vivo* toxicity are provided. This material is available free of charge via the Internet at http://pubs.acs.org.

AUTHOR INFORMATION

Corresponding Author

kataoka@bmw.t.u-tokyo.ac.jp

Author Contributions

◆These authors contributed equally.

Notes

The authors declare no competing financial interest.

ACKNOWLEDGMENTS

This research was supported by the Funding Program for World-Leading Innovative R&D on Science and Technology (FIRST Program) from the Japan Society for the Promotion of Science (JSPS) and Grants-in-Aid for Scientific Research from the Japanese Ministry of Health, Labour and Welfare.

REFERENCES

(1) Davis, M. E.; Chen, Z.; Shin, D. M. *Nat. Rev. Drug Discovery* **2008**, *7*, 771.
(2) Peer, D.; Karp, J. M.; Hong, S.; Farokhzad, O. C.; Margalit, R.; Langer, R. *Nat. Nanotechnol.* **2007**, *2*, 751.
(3) Duncan, R. *Curr. Opin. Biotechnol.* **2011**, *22*, 492.
(4) Nishiyama, N.; Kataoka, K. *Pharmacol. Ther.* **2006**, *112*, 630.
(5) Miyata, K.; Christie, R. J.; Kataoka, K. *React. Funct. Polym.* **2011**, *7*, 227.
(6) Matsumura, Y.; Maeda, H. *Cancer Res.* **1986**, *46*, 6387.
(7) Allen, T. M. *Nat. Rev. Cancer* **2002**, *2*, 750.
(8) Torchilin, V. *Expert Opin. Drug Deliv.* **2008**, *5*, 1003.
(9) Cheng, W. W.; Allen, T. M. *Expert Opin Drug Delivery* **2010**, *7*, 461.
(10) Farokhzad, O. C.; Cheng, J.; Teply, B. A.; Sherifi, I.; Jon, S.; Kantoff, P. W.; Richie, J. P.; Langer, R. *Proc. Natl. Acad. Sci. U.S.A.* **2006**, *103*, 6315.
(11) Zhang, X.-X.; Eden, H. S.; Chen, X. *J. Controlled Release* **2012**, *159*, 2.
(12) Oba, M.; Vachutinsky, Y.; Miyata, K.; Kano, M. R.; Ikeda, S.; Nishiyama, N.; Itaka, K.; Miyazono, K.; Koyama, H.; Kataoka, K. *Mol. Pharmaceutics* **2010**, *7*, 501.
(13) Bae, Y.; Jang, W. D.; Nishiyama, N.; Fukushima, S.; Kataoka, K. *Mol. Biosyst.* **2005**, *1*, 242.
(14) Hakomori, S. *Cancer Res.* **1996**, *56*, 5309.
(15) Dube, D. H.; Bertozzi, C. R. *Nat. Rev. Drug Discovery* **2006**, *4*, 477.
(16) Xu, Y.; Sette, A.; Sidney, J.; Gendler, S. J.; Franco, A. *Immunol. Cell Biol.* **2005**, *83*, 440.
(17) Kannagi, R.; Sakuma, K.; Miyazaki, K.; Lim, K. T.; Yusa, A.; Yin, J.; Izawa, M. *Cancer Sci.* **2010**, *101*, 586.
(18) Kannagi, R.; Izawa, M.; Koike, T.; Miyazaki, K.; Kimura, N. *Cancer Sci.* **2004**, *95*, 377.
(19) Sharon, N. *J. Biol. Chem.* **2007**, *282*, 2753.
(20) Koprowski, H.; Herlyn, M.; Steplewski, Z.; Sears, H. F. *Science* **1981**, *212*, 53.
(21) Durocher, J. R.; Payne, R. C.; Conrad, M. E. *Blood* **1975**, *45*, 11.
(22) Born, G. V.; Palinski, W. *Br. J. Exp. Pathol.* **1985**, *66*, 543.
(23) Matsumoto, A.; Cabral, H.; Sato, N.; Kataoka, K.; Miyahara, Y. *Angew. Chem., Int. Ed.* **2010**, *49*, 5494.
(24) Otsuka, H.; Uchimura, E.; Koshino, H.; Okano, T.; Kataoka, K. *J. Am. Chem. Soc.* **2003**, *125*, 3493.
(25) Djanashvili, K.; Frullano, L.; Peters, J. A. *Chem.—Eur. J.* **2005**, *11*, 4010.
(26) Geninatti Crich, S.; Alberti, D.; Szabo, I.; Aime, S.; Djanashvili, K. *Angew. Chem., Int. Ed.* **2013**, *52*, 1161.
(27) Kataoka, K.; Harada, A.; Nagasaki, Y. *Adv. Drug Delivery Rev.* **2001**, *47*, 113.
(28) Osada, K.; Christie, R. J.; Kataoka, K. *J. R. Soc. Interface* **2009**, *6*, S325.
(29) Cabral, H.; Kataoka, K. *Sci. Technol. Adv. Mater.* **2010**, *11*, 014109.
(30) Matsumura, Y.; Kataoka, K. *Cancer Sci.* **2009**, *100*, 572.
(31) Plummer, R.; Wilson, R. H.; Calvert, H.; Boddy, A. V.; Griffin, M.; Sludden, J.; Tilby, M. J.; Eatock, M.; Pearson, D. G.; Ottley, C. J.; Matsumura, Y.; Kataoka, K.; Nishiya, T. *Br. J. Cancer* **2011**, *104*, 593.
(32) Cabral, H.; Nishiyama, N.; Okazaki, S.; Koyama, H.; Kataoka, K. *J. Controlled Release* **2005**, *101*, 223.
(33) Cabral, H.; Nishiyama, N.; Kataoka, K. *J. Controlled Release* **2007**, *121*, 146.
(34) Murakami, M.; Cabral, H.; Matsumoto, Y.; Wu, S.; Kano, M. R.; Yamori, T.; Nishiyama, N.; Kataoka, K. *Sci. Transl. Med.* **2011**, *3*, 64ra2.
(35) Cabral, H.; Matsumoto, Y.; Mizuno, K.; Chen, Q.; Murakami, M.; Kimura, M.; Terada, Y.; Kano, M. R.; Miyazono, K.; Uesaka, M.; Nishiyama, N.; Kataoka, K. *Nat. Nanotechnol.* **2011**, *6*, 815.
(36) Kinoshita, Y.; Sato, S.; Takeuchi, T. *Cell. Struct. Funct.* **1989**, *14*, 35.
(37) Springsteen, G.; Wang, B. *Tetrahedron* **2002**, *58*, 5291.
(38) Levonis, S. M.; Kiefel, M. J.; Houston, T. A. *Chem. Commun.* **2009**, *17*, 2278.
(39) Teichert, J. F.; Mazunin, D.; Bode, J. W. *J. Am. Chem. Soc.* **2013**, *135*, 11314.
(40) Regueiro-Figueroa, M.; Djanashvili, K.; Esteban-Gómez, D.; de Blas, A.; Platas-Iglesias, C.; Rodríguez-Blas, T. *Eur. J. Org. Chem.* **2010**, 3237.
(41) DiCesare, N.; Lakowicz, J. R. *J. Phys. Chem. A* **2001**, *105*, 6834.
(42) Sun, X.-Y.; Liu, B.; Jiang, Y.-B. *Anal. Chim. Acta* **2004**, *515*, 285.
(43) Martin, G. R.; Jain, R. K. *Cancer Res.* **1994**, *54*, 5670.
(44) James, T. D.; Sandanayake, K. R. A. S.; Shinkai, S. *Nature* **1995**, *374*, 345.
(45) James, T. D.; Sandanayake, K. R. A. S.; Shinkai, S. *Angew. Chem., Int. Ed.* **1996**, *35*, 1919.
(46) Mori, Y.; Suzuki, A.; Yoshino, K.; Kakihana, H. *Pigm. Cell Res.* **1989**, *2*, 273.
(47) Tomsho, J. W.; Benkovic, S. J. *J. Org. Chem.* **2012**, *77*, 2098.
(48) Miller, A.; Sullivan, J. F.; Katz, J. H. *Cancer Res.* **1963**, *23*, 485.
(49) Gatenby, R. A.; Gillies, R. J. *Nat. Rev. Cancer* **2004**, *4*, 891.
(50) Graham, M. A.; Lockwood, G. F.; Greenslade, D.; Brienza, S.; Bayssas, M.; Game, E. *Clin. Cancer Res.* **2000**, *6*, 1205.

Cyclic RGD-Linked Polymeric Micelles for Targeted Delivery of Platinum Anticancer Drugs to Glioblastoma through the Blood–Brain Tumor Barrier

Yutaka Miura,[†,‡,§] Tomoya Takenaka,[†] Kazuko Toh,[§] Shourong Wu,[§] Hiroshi Nishihara,[△] Mitsunobu R. Kano,[∥] Yasushi Ino,[⊥] Takahiro Nomoto,[#] Yu Matsumoto,[§] Hiroyuki Koyama,[‡] Horacio Cabral,[#] Nobuhiro Nishiyama,[○,*] and Kazunori Kataoka[†,◇,§,*]

[†]Department of Materials Engineering, Graduate School of Engineering, The University of Tokyo, 7-3-1 Hongo, Bunkyo-ku, Tokyo 113-8656, Japan, [‡]Division of Tissue Engineering, Graduate School of Medicine, The University of Tokyo, 7-3-1 Hongo, Bunkyo-ku, Tokyo 113-8655, Japan, [§]Center for Disease Biology and Integrative Medicine, Graduate School of Medicine, The University of Tokyo, 7-3-1 Hongo, Bunkyo-ku, Tokyo 113-0033, Japan, [△]Department of Translational Pathology, Graduate School of Medicine, Hokkaido University, N15W7, Kita-ku, Sapporo 060-8638, Japan, [∥]Department of Pharmaceutical Biomedicine, Graduate School of Medicine, Dentistry, and Pharmaceutical Science, Okayama University, 1-1-1 Tsushima-naka, Kita-ku, Okayama 700-8530, Japan, [⊥]Division of Innovative Cancer Therapy, The Institute of Medical Science, The University of Tokyo, 4-6-1 Shirokanedai, Minato-ku, Tokyo 108-8639, Japan, [#]Department of Bioengineering, Graduate School of Engineering, The University of Tokyo, 7-3-1 Hongo, Bunkyo-ku, Tokyo 113-8656, Japan, [○]Polymer Chemistry Division, Chemical Resources Laboratory, Tokyo Institute of Technology, R1-11, 4259 Nagatsuta, Midori-ku, Yokohama 226-8503, Japan, and [◇]Center for NanoBio Integration, The University of Tokyo, 7-3-1 Hongo, Bunkyo-ku, Tokyo 113-8656, Japan

ABSTRACT Ligand-mediated drug delivery systems have enormous potential for improving the efficacy of cancer treatment. In particular, Arg-Gly-Asp peptides are promising ligand molecules for targeting $\alpha_v\beta_3/\alpha_v\beta_5$ integrins, which are overexpressed in angiogenic sites and tumors, such as intractable human glioblastoma (U87MG). We here achieved highly efficient drug delivery to U87MG tumors by using a platinum anticancer drug-incorporating polymeric micelle (PM) with cyclic Arg-Gly-Asp (cRGD) ligand molecules. Intravital confocal laser scanning microscopy revealed that the cRGD-linked polymeric micelles (cRGD/m) accumulated rapidly and had high permeability from vessels into the tumor parenchyma compared with the PM having nontargeted ligand, "cyclic-Arg-Ala-Asp" (cRAD). As both cRGD/m- and cRAD-linked polymeric micelles have similar characteristics, including their size, surface charge, and the amount of incorporated drugs, it is likely that the selective and accelerated accumulation of cRGD/m into tumors occurred *via* an active internalization pathway, possibly transcytosis, thereby producing significant antitumor effects in an orthotopic mouse model of U87MG human glioblastoma.

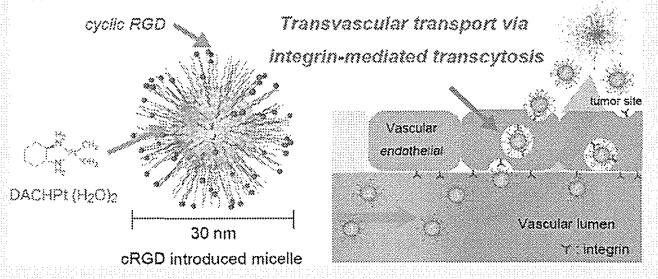

KEYWORDS: drug delivery · block copolymer · polymeric micelle · integrin · cRGD · cancer therapy

Treatment of glioblastoma (GBM) is one of the greatest challenges in cancer therapy.[1−4] Although a large number of advanced treatment paradigms have had impacts on medical management for other tumors, prolongation of GBM patients' survival has not been achieved in decades.[5−9] Because of the difficulty of complete surgical excision, irradiation and chemotherapy play important roles in conventional GBM treatment. However, the effects of chemotherapy on GBM are very limited as a result of poor drug penetration from vessels into tumors caused by the vascular/tumor barrier such as the blood–brain barrier (BBB) and the blood–brain tumor barrier (BBTB).[10−15] In fact, the vascular/tumor barrier is highly variable and heterogeneous in the brain. At the early stage of GBM, the tumor cells use the normal brain vessels, which are protected by the BBB, for their growth.[11,13−17] The gradual progression of GBM and its neovascularization compromise the integrity of BBB and lead to the formation of BBTB.[11,16,17] By the time GBM is diagnosed,

* Address correspondence to kataoka@bmw.t.u-tokyo.ac.jp; nishiyama@res.titech.ac.jp.

Received for review May 27, 2013 and accepted September 12, 2013.

Published online September 12, 2013
10.1021/nn402662d

the tumor has already developed neovasculature and the BBTB is presented. Therefore, it is important to deliver the effective dose of therapeutic agents into tumor tissues through the BBTB. In the clinic, chemotherapeutic agents may be administrated at high concentrations to circumvent the BBTB,[18] although this strategy is always jeopardized by side effects. Thus, alternative approaches are needed to overcome the BBTB and to transport therapeutic agents efficiently to brain tumors using smart drug delivery systems (DDSs).[19−25]

In general, the main driving force for tumor accumulation of drug carriers can be explained by the enhanced permeability and retention (EPR) effect, which is characterized by microvascular hyperpermeability to circulating macromolecules and impaired lymphatic drainage in tumor tissues.[26] However, the presence of the BBTB limits the EPR effect, thereby resulting in the poor efficacy in drug delivery to GBM.[17,27] A feasible approach for overcoming this issue is the use of ligands that facilitate the translocation of drug carriers across the endothelium of the tumor vasculature. Here, we focused on cyclic Arg-Gly-Asp (cRGD)[25] as a candidate ligand because this cyclic peptide has selective affinity for the $\alpha_v\beta_3$ and $\alpha_v\beta_5$ integrins that are overexpressed on the endothelial cells of tumor angiogenic vessels[28,29] as well as on GBM cells (*e.g.*, the U87MG cell line)[30−32] and because cRGD-linked nanocarriers have shown therapeutic efficacy in GBM.[33,34] However, the mechanisms for the accumulation of cRGD-linked nanocarriers in GBM are still controversial. In this regard, we have recently demonstrated the spatiotemporal and quantitative analyses of extravasation, tissue penetration, and cellular internalization of drug carriers in a living animal through the intravital confocal laser scanning microscopy (IVCLSM) technique.[35−38] Thus, we adapted this technique to long-circulating cRGD-linked nanocarriers for studying the penetration pathway and the derived therapeutic activity of cRGD-mediated DDS. To our knowledge, no systematic research exists addressing the *in situ* observation of translocating behavior of the drug-incorporated cRGD nanocarriers crossing the vascular barrier, and mechanisms involved in cRGD-induced transvascular transport have not been clearly proven yet.

We here developed new long-circulating, cyclic RGD-linked polymeric micelles (PMs) incorporating (1,2-diaminocyclohexane)platinum(II) (DACHPt), the parent complex of the potent anticancer drug oxaliplatin, through the metal complex formation-driven self-assembly of poly(ethylene glycol) (PEG)-*b*-poly(L-glutamic acid) and DACHPt in an aqueous milieu (DACHPt/m).[35,39,40] A series of cRGD-linked DACHPt/m (cRGD/m) was prepared with various cRGD conjugation ratios, ranging from 5% to 40%, in the distal ends of the PEG strands in the outer-shell layer of the PMs. We compared their antitumor effects against GBM with a control DACHPt/m linked with the nontargeted

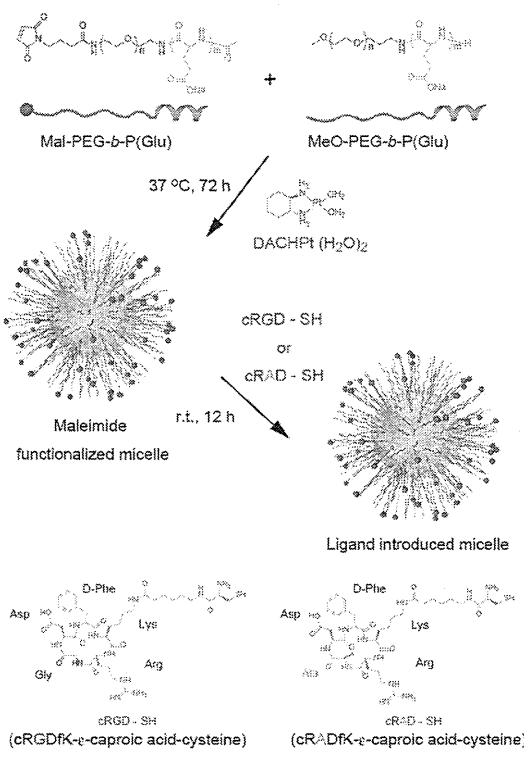

Figure 1. Schematic showing the design and synthesis strategy for the ligand-linked DACHPt/m.

peptide cyclic-Arg-Ala-Asp (cRAD). Intravital confocal laser scanning microscopy was used to observe the behaviors of the micelle at tumor sites. This showed that cRGD/m, but not control micelles, could bypass vascular/tumor barriers *in situ* and penetrate deep into GBM through cRGD-induced transvascular transport presumably related to transcytosis, resulting in the induction of potent antitumor effects against malignant glioma.

RESULTS AND DISCUSSION

Development of Surface-Tunable DACHPt/m. cRGD/m with varying densities of cRGD ligand were prepared by "postconjugating" Cys-containing cRGD peptides onto maleimide-functionalized DACHPt/m (the precursor micelle) obtained from a mixture of poly(ethylene glycol)-*b*-poly(L-glutamic acid) (MeO-PEG-*b*-P(Glu)) and maleimide-conjugated poly(ethylene glycol)-*b*-poly(L-glutamic acid) (Mal-PEG-*b*-P(Glu)) (Figure 1). The key features of this strategy are related to the preparation of the precursor micelles, where maleimide functional groups on the micelle surface at a controlled density allow highly reproducible introduction of any ligand molecule with thiol residues. Mal-PEG-*b*-P(Glu) was prepared according to the following scheme. Ring-opening polymerization of the *N*-carboxy anhydride of γ-benzyl L-glutamate with NH_2-PEG-N_3 yielded the azido-terminated diblock copolymer N_3-poly(ethylene glycol)-*b*-poly(γ-benzyl L-glutamate) (N_3-PEG-*b*-PBLG), which was followed by the removal of the γ-benzyl side chain under

TABLE 1. Characterization of (1,2-Diaminocyclohexane)platinum(II) (DACHPt)-Loaded Micelles

micelles	cRGD[a,e] (%)	cRAD[a,f] (%)	size[b] (nm)	PDI[b,g]	[Pt]/[COO][c] (mol/mol)	zeta potential[d] (mV)
ctrl/m[h]	0	0	27	0.096	0.51	−3.1 ± 0.5
5% cRGD/m[i]	5 ± 2	0	28	0.088	0.50	−3.4 ± 0.3
10% cRGD/m	10 ± 2	0	30	0.100	0.55	−2.8 ± 0.7
20% cRGD/m	22 ± 2	0	29	0.099	0.52	−2.3 ± 0.4
40% cRGD/m	43 ± 2	0	31	0.093	0.49	−2.9 ± 0.3
20% cRAD/m[j]	0	20 ± 2	31	0.101	0.54	−2.5 ± 0.7

[a] Determined by ^{1}H NMR. [b] Determined by DLS. [c] Determined based on ICP-MS measurements of platinum concentration and the weight of dried micelles. [d] Determined by laser Doppler electrophoresis (n = 4, mean ± SD). [e] cRGD, cyclic Arg-Gly-Asp. [f] cRAD, cyclic Arg-Ala-Asp. [g] PDI, polydispersity. [h] ctrl/m, control DACHPt/m. [i] cRGD/m, cRGD-linked DACHPt/m. [j] cRAD/m, cRAD-linked DACHPt/m.

alkali conditions to obtain N_3-PEG-*b*-P(Glu). The α-end azido group of N_3-PEG-*b*-P(Glu) was then reduced to a primary amino group and reacted further with *N*-(4-maleimidobutyryloxy)sulfosuccinimide (sulfo-GMBS) to obtain Mal-PEG-*b*-P(Glu) (Supporting Information Figure S1). By controlling the ratio of MeO-PEG-*b*-P(Glu)/Mal-PEG-*b*-P(Glu), a series of surface-tunable micelles with different percentages of maleimide groups on their surfaces was prepared before cyclo[RGDfK(CX-)] (cRGD peptide, X = 6-aminocaproic acid, ε-Acp) was introduced onto the DACHPt/m surface *via* Michael addition reactions. This strategy facilitated the preparation of DACHPt micelles with 5−40% cRGD ligands (Table 1). These percentages, which represent the molarities of ligand molecules on the DACHPt/m surface, were determined by ^{1}H nuclear magnetic resonance (NMR) spectroscopy (Supporting Information).

Cyclo[RADfK(CX-)] (cRAD peptide, X = ε-Acp) was also used as a nontargeting ligand molecule. As described in detail later, 20% cRGD-linked DACHPt/m had the best potential for *in vitro* activity. Thus, we prepared 20% cRAD-linked DACHPt/m as a nontargeting-ligand-linked micelle, which was used as a control micelle for comparison. In all cases, the ligand-linked micelles prepared in this study had similar characteristics (Table 1). Even after modifying the surface, all the micelles produced had diameters between 27 and 31 nm with narrow polydispersity (PDI). Therefore, it was appropriate to verify the effect of ligands by using these micelles.

Integrin-Dependent Activity of Ligand-Linked DACHPt/m in Tumor Cells. To evaluate the biological activities of the ligand-linked micelles, we quantitatively analyzed their cellular uptake in $\alpha_v\beta_3$- and $\alpha_v\beta_5$-positive U87MG human GBM cells by inductively coupled plasma mass spectrometry (ICP-MS) (Figure 2a). Free oxaliplatin was taken up continuously by the U87MG cells, whereas control DACHPt/m (ctrl/m, without ligand molecules) was internalized slowly *via* endocytosis.[36] In contrast, higher cellular uptake of cRGD/m was observed in the early stages of the experiment, particularly when the amount of cRGD was increased (Figure 2a). With 20% and 40% cRGD/m, the internalized platinum amount was approximately 2.5-fold higher than that with 20% cRAD-linked DACHPt/m (20% cRAD/m) after 3 h incubation (Figure 2a). Thus, we prepared a fluorescence (Alexa 555)-labeled PM (Supporting Information) to perform *in vitro* confocal laser scanning microscopy (CLSM). The results showed that the 20% cRGD/m was taken up rapidly into the U87MG cells, whereas the ctrl/m and 20% cRAD/m were internalized more gradually (Figure 2b). On the basis of the CLSM images, the quantification of cell-associated fluorescence was consistent with the ICP-MS data (Figure 2c). As shown in Figure 3a, the introduction of cRGD ligands increased the *in vitro* cytotoxicity of DACHPt/m. The results obtained 48 h after incubation (white bar in Figure 3a) showed that 50% growth inhibitory concentration (IC_{50}) values were lower with 20% and 40% cRGD/m. Due to the cRGD-associated cellular uptakes (Figure 2a), this tendency was enhanced when the cytotoxicity assay method was changed to a 3 h drug/micelle exposure, followed by 48 h postincubation (gray bar in Figure 3a). These results suggested that the ligand density was essential for increasing the cytotoxicity of micelles. To confirm the recognition of integrins by the cRGD ligand, we established α_v integrin downregulated U87MG cells by RNA silencing (Supporting Information Figure S2a and b). Flow cytometric analysis revealed that the U87MG cells expressed $\alpha_v\beta_3$ (blue line) and $\alpha_v\beta_5$ (red line) integrins, whereas the α_v integrin-downregulated U87MG cells expressed almost no $\alpha_v\beta_3$ and $\alpha_v\beta_5$ integrins (Figure 4a and b). *In vitro* cytotoxicity assays using integrin-downregulated U87MG cells showed that the activity of cRGD/m was changed to similar values of both ctrl/m and 20% cRAD/m, thereby indicating a crucial role for binding of cRGD ligands with the $\alpha_v\beta_3$ and $\alpha_v\beta_5$ integrins in the enhanced cytotoxicity of cRGD/m against the U87MG cells (Figure 3b). It should be noted that the recently developed antiangiogenesis drug cilengitide includes a cRGD sequence and has been demonstrated to have antitumor activity against GBM.[30,31,41−45] However, the cytotoxicity of cilengitide itself is very low. For instance, Mikkelsen *et al.* studied the cytotoxicity of cilengitide in combination with X-ray irradiation, but no significant cytotoxicity was observed for 10 μM cilengitide without radiation.[44] In our system, only 2 μM cRGD (in the case of 40% cRGD-linked DACHPt/m solution) is

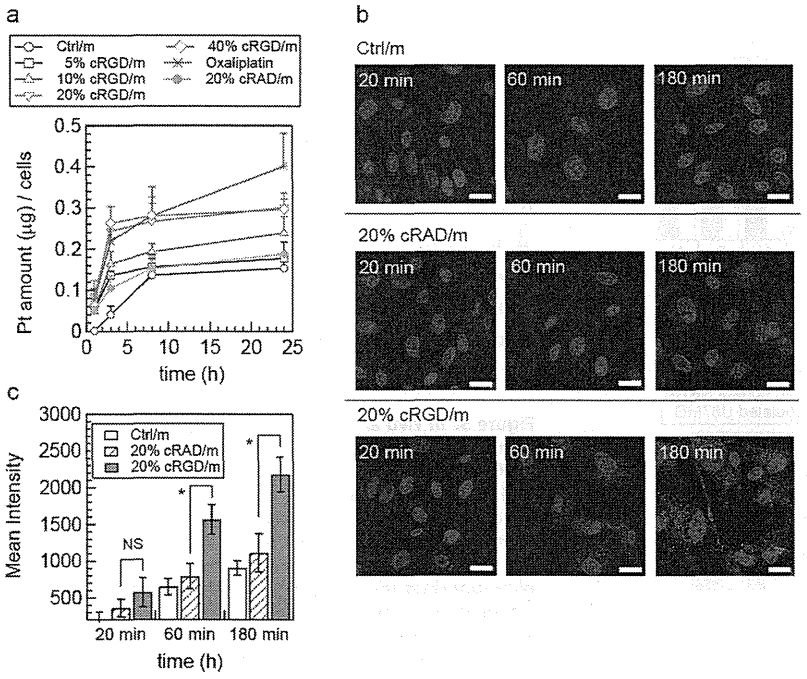

Figure 2. Cellular uptake of DACHPt/m with various ligand species and densities. (a) *In vitro* cellular uptake of micelle-encapsulated platinum, which was determined by ICP-MS. The obtained cell-associated platinum increased as the percentage ligand payload in the micelles increased, whereas ctrl/m remained at low values. Experiments were performed four times in quadruplicate. They produced similar results. Bars represent the mean ± standard error of the mean (SEM). (b) *In vitro* CLSM of Alexa 555-labeled ctrl/m, 20% cRGD/m, and 20% cRAD/m uptake in U87MG glioblastoma cells. The cells were incubated with the respective micelle solutions (10 μM platinum) for 20, 60, and 180 min at 37 °C. All pictures show merged images, which include the nuclei (blue) and micelles (red). Scale bars represent 20 μm in all images. (c) Quantitative analysis of the amount of internalized micelles based on the CLSM results. Thirty different cells were analyzed and evaluated at each time point. Data represent mean ± SEM from three independent experiments performed in triplicate. The data were analyzed using Student's *t*-test, and $*p < 0.001$ was considered significant.

included in 100 μM (based on DACHPt) micelle solution. Thus, the concentrations of cRGD in our micelle did not reach a toxic range. Overall, these results highlight the importance of the ligand density, particularly when the surface payload of peptide ligand molecules on the micelle reached 20–40%, which correlated with the maximum cancer cell uptake and cytotoxicity.

Therapeutic Efficacy and Accumulation Behavior of Ligand-Linked DACHPt/m in Human GBM Models. U87MG tumors have a highly angiogenic vasculature and overexpress integrin receptors, as described above. Thus, our ligand-linked micelle system should be highly suitable for the treatment of GBM models. On the basis of the results of *in vitro* cytotoxicity assays, 20% cRGD ligand-linked DACHPt/m was tested against xenografted U87MG tumor-bearing mice and compared with oxaliplatin and 20% cRAD/m. These mice were treated by systemic injections of micelle solutions every other day (total of three injections), starting 5 days after tumor inoculation. While no inhibition of tumor growth was observed in oxaliplatin-treated tumors (Figure 5a), 20% cRGD-linked micelles demonstrated significant tumor growth inhibition (Figure 5a). Conversely, nontargeting-ligand-linked micelle, cRAD/m, had no therapeutic effect, indicating the sequence specificity of the peptide ligand was essential (Figure 5a). According to previous reports, single-cilengitide treatments with a high dosage of cRGD, such as 2400 mg/m^2, against brain tumor have provided only moderate therapeutic efficacy.[45] Therefore, the antitumor activity that we showed in this study is assumed to be caused by the incorporated DACHPt, not by cRGD. The interesting point here is the tumor-accumulating behavior of cRGD/m, as it revealed a fast accumulation within 4 h after administration (Figure 5b, *ca.* 2.2-fold at 4 h *vs* 20% cRAD/m), followed by the further gradual accumulation until 24 h, despite both micelles showing similar size (Table 1) and comparable blood circulation profiles (Figure 5c). Thus, the tumor-association behavior of cRGD/m is clearly distinct from micelles that can be accumulated into tumors just by the EPR effect, indicating the key features of ligand effects.

To understand the functionality of cRGD/m in a human GBM model, the *in vivo* behaviors of cRGD/m and cRAD/m were comparatively analyzed by IVCLSM. As we reported previously, IVCLSM is a useful technique to reveal blood circulation, extravasation, and tissue penetration of micelles in living animals.[37] Here, cRGD/m and cRAD/m were labeled with Alexa 647 (red) and DyLight 488 (green) fluorescent probes, respectively (Supporting Information), and concurrently injected iv into the U87MG tumor-bearing mice. In this

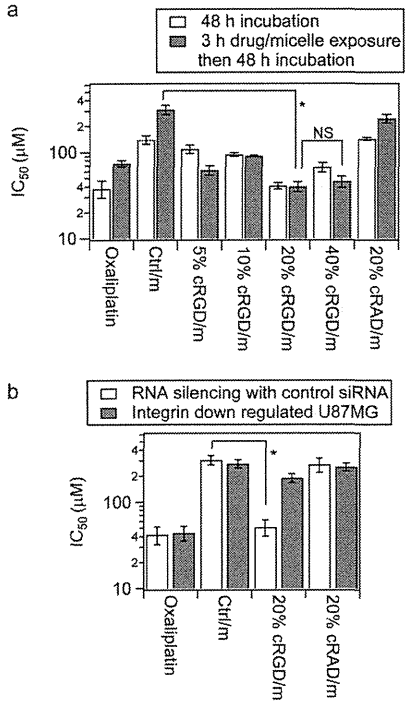

Figure 3. Variation in IC_{50} values with U87MG *in vitro* treatment. (a) *In vitro* cytotoxicities of free oxaliplatin or DACHPt/m with different percentages of ligand molecules in the U87MG cells and (b) *in vitro* cytotoxicities of oxaliplatin, 20% cRGD/m, and 20% cRAD/m in α_v integrin-downregulated U87MG cells (Supporting Information). The IC_{50} values were determined using Cell Counting Kit-8 and are expressed as the percentages of control wells. The experiments were confirmed four times. The data were analyzed using Student's *t*-test, and $*p < 0.001$ was considered significant.

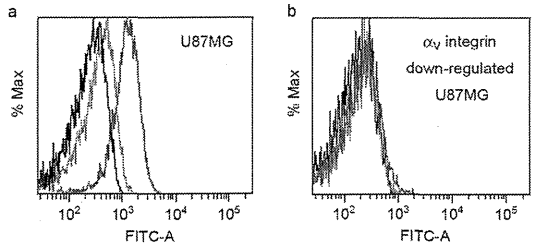

Figure 4. Flow cytometric analysis of integrin expression. (a) U87MG glioblastoma cells and (b) α_v integrin-down-regulated U87MG cells. FITC-labeled mouse IgG: control, black; FITC-labeled anti-$\alpha_v\beta_3$ integrin antibody: blue; and FITC-labeled anti-$\alpha_v\beta_5$ integrin antibody: red.

case, it is possible to evaluate the real-time extravasation and penetration of the micelles based on the changes in fluorescence signals within the same tumor. Figure 6a and b show IVCLSM snapshots of the U87MG tumor site. At 5 min after administration, the color in the bloodstream appeared yellow due to the co-localization of both micelles (Figure 6a). At 5 h after injection, the fluorescence signal corresponding to cRGD/m (red) was clearly observed inside the tumor tissue (Figure 6b). This phenomenon was confirmed by using the opposite combination of fluorescent probes, *i.e.*, DyLight 488-labeled cRGD/m (green) and Alexa

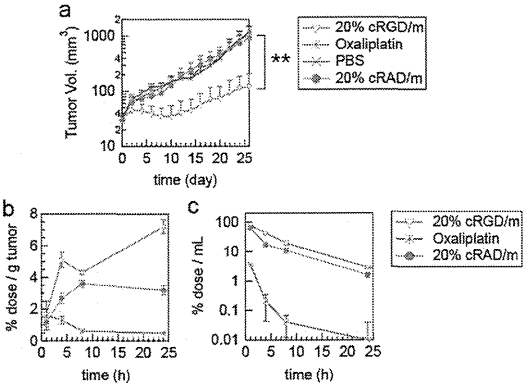

Figure 5. *In vivo* anticancer activity, plasma clearance, and tumor accumulation of cRGD- and cRAD-linked DACHPt/m. (a) Comparison of tumor growth inhibition with cRGD/m and cRAD/m. Five days after tumor cell transplantation, the mice were injected intravenously with micelles. The micelles (4 mg/kg based on DACHPt) were administered every other day (three injections). Oxaliplatin was used as a control platinum drug (dose = 8 mg/kg) with the same treatment schedule. Bars represent mean ± SD (n = 8). Two-way ANOVA was used to analyze the differences in the tumor mass volume, and $**p < 0.001$ was considered significant. (b) Tumor accumulation of DACHPt/m and oxaliplatin. Mice bearing U87MG tumors (n = 6) were injected intravenously with 20% cRGD/m, 20% cRAD/m, and oxaliplatin at 100 μg/mouse on a DACHPt basis. The mice were sacrificed 1, 4, 8, and 24 h after injection. Acid digestion of all tumors was performed using approximately 1.0 mL of concentrated HNO_3 at 200 °C, and the dried samples were dissolved in 1 vol % HNO_3(aq) (1.0 mL). Platinum concentration was measured by ICP-MS. Bars represent mean ± SEM. (c) Plasma clearance of DACHPt/m and oxaliplatin. Blood was collected from the inferior vena cava, heparinized, and centrifuged to obtain the plasma. Acid digestion of all samples was performed using approximately 1.0 mL of concentrated HNO_3 at 200 °C, and the dried samples were dissolved in 1 vol % HNO_3(aq) (1.0 mL). Platinum concentration was measured by ICP-MS. Data represent mean ± SEM (n = 6).

647-labeled cRAD/m (red), and the result indicated the time-dependent increase in the green fluorescence (cRGD/m) at tumor tissue (Figure 6c,d and Supporting Video). To quantitatively evaluate the accumulation of the micelles at the tumor tissue, three different regions were selected (white rectangle in Figure 6c), and the changes in the fluorescence signals were analyzed for up to 9 h. For cRGD/m, a rapid increase in the fluorescence signals (green) in the tumor tissue during the initial 5 h was confirmed (Figure 6e). This observation is well consistent with the ICP-MS results of the tumor accumulation as shown in Figure 5b. Thus, the IVCLSM results indicated that despite the subtle difference in the amino acid sequence, the cRAD peptides were unable to facilitate extravasation and penetration of PMs as could cRGD. Moreover, based on the IVCLSM results (Figure 6c and d), we quantitatively analyzed the permeability of DyLight 488-labeled cRGD/m and Alexa 647-labeled cRAD/m from vasculature to the interstitium of U87MG tumor. The fluorescence intensity in the selected region (blue rectangle in Figure 6c) was observed. As shown in Figure 6f, the strong green